The photodissociation of CH_3I in the red edge of the *A*-band: Comparison between slice imaging experiments and multisurface wave packet calculations

L. Rubio-Lago,[1,2] A. García-Vela,[3] A. Arregui,[1] G. A. Amaral,[1] and L. Bañares[1,a)]
[1]*Departamento de Química Física I, Facultad de Ciencias Químicas, Universidad Complutense de Madrid, Madrid 28040, Spain*
[2]*Instituto de Estructura de la Materia, CSIC, C/Serrano, 123, Madrid 28006, Spain*
[3]*Instituto de Física Fundamental, CSIC, C/Serrano, 123, Madrid 28006, Spain*

(Received 24 August 2009; accepted 10 October 2009; published online 5 November 2009)

The photodissociation of methyl iodide at different wavelengths in the red edge of the *A*-band (286–333 nm) has been studied using a combination of slice imaging and resonance enhanced multiphoton ionization detection of the methyl fragment in the vibrational ground state ($\nu=0$). The kinetic energy distributions (KED) of the produced $CH_3(\nu=0)$ fragments show a vibrational structure, both in the $I(^2P_{3/2})$ and $I^*(^2P_{1/2})$ channels, due to the contribution to the overall process of initial vibrational excitation in the ν_3(C–I) mode of the parent CH_3I. The structures observed in the KEDs shift toward upper vibrational excited levels of CH_3I when the photolysis wavelength is increased. The $I(^2P_{3/2})/I^*(^2P_{1/2})$ branching ratios, photofragment anisotropies, and the contribution of vibrational excitation of the parent CH_3I are explained in terms of the contribution of the three excited surfaces involved in the photodissociation process, $^3Q_0$, $^1Q_1$, and $^3Q_1$, as well as the probability of nonadiabatic curve crossing $^1Q_1 \leftarrow {}^3Q_0$. The experimental results are compared with multisurface wave packet calculations carried out using the available *ab initio* potential energy surfaces, transition moments, and nonadiabatic couplings, employing a reduced dimensionality (pseudotriatomic) model. A general qualitative good agreement has been found between theory and experiment, the most important discrepancies being in the $I(^2P_{3/2})/[I(^2P_{3/2})+I^*(^2P_{1/2})]$ branching ratios. Inaccuracies of the available potential energy surfaces are the main reason for the discrepancies. © *2009 American Institute of Physics*. [doi:10.1063/1.3257692]

I. INTRODUCTION

The photodissociation dynamics of CH_3I attracted considerable attention in the last decades owing to the fact that it combines an interesting dynamics with a high accessibility from a variety of both experimental and theoretical approaches (see Refs. 1 and 2 for recent reviews).

The first absorption band of CH_3I, the *A*-band, consists of a broad featureless continuum ranging from 220 to 350 nm with a maximum at about 260 nm.[3] It is well known that the lowest energy electronic excitation in CH_3I corresponds to a $n \rightarrow \sigma^*$ transition, where a nonbonding *p* electron of iodine is promoted to the lowest energy available antibonding molecular orbital.[4] The spin-orbit (SO) coupling is large due to the presence of the heavy iodine atom and then a SO configuration can be used for the first excited electronic state.[5] Three SO states are accessible through dipole allowed transitions from the ground state. The $^3Q_1$ and $^1Q_1$ states (in Mulliken's notation[6]) through weak perpendicular transitions and the $^3Q_0$ state through a strong parallel transition.[7] Only the $^3Q_0$ state correlates adiabatically with $CH_3(\tilde{X}\,^2A_2)+I^*(^2P_{1/2})$ products, while the $^3Q_1$ and $^1Q_1$ states correlate with $CH_3(\tilde{X}\,^2A_2)+I(^2P_{3/2})$. A curve crossing between the $^1Q_1$ and $^3Q_0$ states complicates the origin of the $I(^2P_{3/2})$ fragments, since, in principle, they can be produced both adiabatically and nonadiabatically.[8]

The concerted theoretical and experimental efforts unraveled that most of the absorption can be attributed to the $^3Q_0$ state (78% of the total absorption).[3] At the center of the absorption band, the parallel transition to the $^3Q_0$ state, which has its maximum absorption at 261 nm, dominates the absorption spectrum; at higher wavelengths the perpendicular transitions to the $^3Q_1$ state, whose maximum is located around 300 nm, gains in importance, raising its relative absorption strength to ~25% at 304 nm.[3,9]

The analysis of the angular distribution of the photofragments provides a measurement of the strength of the $^1Q_1 \leftarrow {}^3Q_0$ curve crossing. In the adiabatic picture, a pure perpendicular distribution (characterized by an anisotropy parameter $\beta=-1$) is expected for the $CH_3(\tilde{X}\,^2A_2)+I(^2P_{3/2})$ channel, whereas a pure parallel distribution (characterized by an anisotropy parameter $\beta=2$) is expected for the $CH_3(\tilde{X}\,^2A_2)+I^*(^2P_{1/2})$ channel. Instead, early experimental studies at 266 nm reported parallel distributions for both dissociation channels, pointing out that most of the $CH_3(\tilde{X}\,^2A_2)+I(^2P_{3/2})$ products come from the $^1Q_1 \leftarrow {}^3Q_0$ curve crossing.[8,10] Shapiro predicted that the curve crossing probability increases with decreasing energy.[11] This effect was attributed to the fact that at increasing wavelengths, the

a)Electronic mail: banares@quim.ucm.es.

passage through the crossing region slows down, and consequently, a greater crossing probability is expected.

Many experimental efforts have been done to solve the problem of achieving an accurate determination of the $I^*(^2P_{1/2})/[I^*(^2P_{1/2})+I(^2P_{3/2})]$ branching ratio and its dependence on the excitation energy (from now on we will use I^* and I to refer to $I^*(^2P_{1/2})$ and $I(^2P_{3/2})$, respectively, and CH_3 to refer to $CH_3(\tilde{X}\,^2A_2)$). The list includes time-of-flight (TOF) mass spectrometry (TOFMS)[8,12,13] state-selective ionization and pulsed-field TOFMS,[14] vacuum absorption,[15] laser induced fluorescence,[16,17] IR emission,[18–20] photoacoustic spectroscopy,[21,22] gain versus absorption spectroscopy,[23] resonance enhanced multiphoton ionization (REMPI),[24,25] velocity map ion imaging,[26,27] pulsed core-sampling photofragment translational spectroscopy,[28,29] and diode laser spectroscopy.[30,31] Most of the measurements have been carried out around the center of the *A*-band, at $\lambda=266$ and 248 nm, due to the availability of suitable lasers at these wavelengths. In both cases, the measured values lie between 0.70 and 0.81, with an overall spread of the measured data of ~10%. In the most complete study reported up to the date, Eppink and Parker[26,27] scanned the region between 240 and 333 nm. The measured $I^*/[I^*+I]$ branching ratios take an approximate constant value of ~0.9 at wavelengths below 300 nm, and decrease rapidly at higher wavelengths, reaching a value close to ~0.1 at 333 nm. The anisotropy parameters, also reported, confirm a pure parallel mechanism for the CH_3+I^* channel for all the wavelengths studied, while the CH_3+I channel reflects the dual mechanism involved: below 300 nm the reported β takes a value above 1.5, characteristic of a dominant parallel absorption; at higher wavelengths, β drops to zero, reflecting the mixing of the perpendicular absorption via the $^3Q_1$ state and the parallel $^1Q_1 \leftarrow {}^3Q_0$.

The distribution of the dissociation excess energy among the different photofragment degrees of freedom (DOF) focused the attention of many experimental and theoretical works.[10,12,20,26–29,32–39] About 90% of the available energy is channeled into kinetic energy, although a substantial vibrational excitation of the umbrella mode (ν_2) of CH_3 has been observed. In particular, the CH_3+I channel shows vibrational population inversion, in contrast with what is observed in the CH_3+I^*, where the most populated vibrational state is $v=0$.[26–29,35–39] Some experiments have also shown some vibrational excitation of the CH_3 symmetric stretch mode (ν_1).[26–29] Rotational excitation of the CH_3 fragment is also larger for the CH_3+I^* channel than for the CH_3+I channel.

Theoretical studies on the photodissociation dynamics of CH_3I in the *A*-band are strongly coupled with the *ab initio* calculations on the electronic structure, developed in parallel to the experimental work. From a theoretical point of view, CH_3I is an attractive system because it has the advantage of being a quasilinear system, but has more complex vibrational motions than a simple linear triatomic molecule. Furthermore, its photodissociation dynamics mainly involves a parallel transition and the C_3 symmetry axis is highly preserved. The possible vibrational modes excited in the methyl fragment are reduced to two: the symmetric stretch, ν_1, and the umbrella mode, ν_2. The accepted dissociation mechanism is a prompt bond breakage, very fast and directed along the symmetry axis, so very little rotational excitation is expected.

The first theoretical studies on the photodissociation of the CH_3I were based on the model of Shapiro and Bersohn.[40] In this model, the dissociation reaction happens in linear configurations and the umbrella motion of the CH_3 fragment is treated as a C–X stretch mode, where X is a hypothetical atom located in the center of mass (CM) of the H_3. In the first studies, empirical potential surfaces that were built to agree with the measured absorption spectrum and vibrational distributions of the CH_3 fragment were used. Later models[11,41] used two diabatic potential surfaces and a radial nonadiabatic coupling term to reproduce the two observed dissociation channels. A significant advance on the theoretical understanding of the CH_3I system came with the *ab initio* calculations by Amatatsu *et al.*[42] and the construction of the corresponding potential energy surfaces for the two main states ($^3Q_0$ and $^1Q_1$) involved in the photodissociation, first in six dimensions and later in full nine dimensions.[43] These potential surfaces were used in classical trajectory[42,43] and wave packet calculations.[37,39,44] Improved potential energy surfaces were produced by Xie *et al.*[45] based on contracted SO configuration interaction calculations using a better basis set and more spin-free configurations, in order to better reproduce the absorption spectrum of CH_3I. These improved potential surfaces were used in reduced dimensionality wave packet calculations of rotationally selected CH_3I and CD_3I (Ref. 45) and, more recently, focusing on time-resolved properties.[2,46] Recently, Alekseyev *et al.*[1,47] employed larger atomic basis sets and a larger configuration interaction treatment to recalculate the $\tilde{X}\,^1A_1$ ground state and the low-lying excited states, $^3Q_1$, $^3Q_0$, and $^1Q_1$, together with the transition moments relevant to the photodissociation of CH_3I in the *A* band, with the aim of improving the agreement between the experimental and calculated absorption spectra.

In the present work we focused on the photodissociation dynamics of CH_3I in the red edge of the *A* absorption band (286–333 nm). In particular, the reddest wavelength we studied is 333.45 nm, which coincides with the wavelength employed for 2+1 REMPI detection of the $CH_3(\nu=0)$ fragment through the *Q* branch of the $3p_z(^2A_2 \leftarrow {}^2A_2)\ 0_0^0$ transition for a two-photon process (i.e., a one-laser experiment). The photodissociation of CH_3I at this wavelength was first studied by Fairbrother *et al.*[24] in a one-laser experiment by using TOFMS and REMPI detection of the CH_3 fragment. From the arrival time profiles of the CH_3^+ ions measured at different linear polarizations of the photolysis (and detection) laser, they found that at this wavelength the photolysis of CH_3I involves a transition with significant parallel and perpendicular character. They were able to observe both I and I^* channels and deduced that both the $^3Q_0$ and $^3Q_1$ potential energy surfaces are involved in the production of $CH_3(\nu=0)$ in correlation with I atoms. In addition, they provided an upper limit for the conical intersection between the $^3Q_0$ and $^1Q_1$ potential surfaces of $\approx 30\,500$ cm^{-1} and concluded that a contribution from the $^3Q_1$ state to the long wavelength absorption of CH_3I should be considered in future theoretical modeling of this system. Eppink and Parker[26] observed that

the images measured toward the photolysis wavelength 333 nm show nearly pure I channel (with a I^* quantum yield lower than 0.1), but the anisotropy parameter close to zero indicates still a large parallel contribution in the initial absorption, which subsequently undergoes curve crossing.

A good theoretical description of the red edge of the *A* absorption band of CH_3I is a challenge both for electronic structure calculations of the potential energy surfaces involved[47] and for quantum dynamics calculations. In this work, we present an effort directed to understand the involvement of different potential energy surfaces with different parallel and perpendicular characters and the presence of a conical intersection influencing the dynamics in a region of a very weak absorption cross section. High resolution slice imaging experiments are directly compared with the results of multisurface wave packet calculations including all relevant potential energy surfaces and nonadiabatic transitions. The analysis of the experimental kinetic energy and angular distributions of the produced $CH_3(\nu=0)$ fragment in correlation with I and I^* atoms, in combination with this multisurface wave packet calculations, allows an unprecedented detailed description of the photodissociation dynamics of CH_3I in terms of the contribution of the three excited surfaces involved in the process, $^3Q_1$, $^3Q_0$, and $^1Q_1$, as well as the probability of nonadiabatic curve crossing $^1Q_1 \leftarrow {}^3Q_0$.

The paper is organized as follows. In Secs. II and III, the experimental and theoretical methods are presented. Sections IV and V describe the most relevant experimental and theoretical results. A discussion is presented in Sec. VI and, finally, Sec. VII is dedicated to present the most important conclusions of the work.

II. EXPERIMENTAL

The imaging experiments presented here have been performed in a recently improved velocity map imaging setup adapted to the slice imaging technique. With the traditional velocity mapping technique,[48] an inversion method is needed to process the raw crushed images in order to recover the three-dimensional (3D) product speed distribution from the two-dimensional (2D) projection. In contrast with the slice imaging technique, the 3D distribution is directly obtained from the sliced images,[49] without the artificial noise introduced by the transform methods and an enhanced energy resolution in relation to that achieved with the velocity mapping technique. We used delayed pulsed extraction slicing[50] in the single field configuration developed by Kitsopoulos and Papadakis and described in detail in Ref. 51. Briefly, the delayed pulsed extraction allows the ion cloud to spread in velocities so that the arrival time of the ion packet at the detector has a width of several hundreds of nanoseconds. By using a narrow detector time gate of a few nanoseconds, we were able to image only the center slice of the ion packet. In the single field configuration, only two electrodes are used. Unlike previous velocity mapping and slicing methods where the focusing condition is obtained by adjusting the voltage on the second field ion lens, in the single field configuration, the focusing condition is met when the starting position along TOF axis is at a specific distance from either the repeller or the extractor.

A molecular beam is created by expanding a gas mixture of CH_3I in He (10%, 1 atm backing pressure) into vacuum using a pulsed nozzle (General Valve Series 9, 0.5 mm orifice). The gas pulse passes through a skimmer (Beam Dynamics Standard Model 2, 0.5 mm orifice) and is intersected at right angles by the photolysis laser beam. The experiments were performed at 286.16, 305, 310, 315, 325, and 333.45 nm to cover the red edge of the *A*-band absorption of CH_3I. Two different types of pump-and-probe schemes were used. In the experiments carried out at 305, 310, 315, and 325 nm, the photolysis laser consists of a MOPO laser (Spectra-Physics 730D10) pumped by a neodymium-doped yttrium aluminum garnet (Nd:YAG) laser (Quanta Ray Pro Series 230) at 355 nm. The resulting radiation of typically $\approx$500 μJ per pulse was focused into the reaction chamber with a lens of 25 cm focal length. The CH_3 fragments produced are ionized 10 ns later with a focused (30 cm focal length) probe pulse of $\approx$1.5 mJ generated by a Nd:YAG (Quanta Ray Pro Series 190) pumped frequency doubled dye laser (SIRAH). The probe laser wavelength was set at 333.45 nm, centered at the *Q* branch of the $3p_z(^2A_2 \leftarrow {}^2A_2)$ 0_0^0 transition for a two-photon process. In the experiments carried out at the photolysis wavelengths of 286 and 333.45 nm, coincident with REMPI) transitions of the methyl fragment (the *Q* branch of the $4p_z(^2A_2 \leftarrow {}^2A_2)$ 0_0^0 transition is located at 286.15 nm), the temporal width of the pulses ($\approx$10 ns) allows us to use the same laser pulse as pump and probe (one-laser experiments). In the two-color two-laser experiments, the probe laser energy was kept as low as possible in order to have the minimum single laser contribution. Background images in the same condition than the pump-and-probe data were taken alternatively and later on subtracted prior to the image integration.

The generated ions are accelerated by the ion optics and pass through a field-free TOF region before hitting the impedance matched microchannel plates (MCPs) (Chevron configuration, 40 mm diameter). The gain of the MCPs can be gated with a high voltage pulse to allow only the ions of interest to be detected. The resulting electron avalanche strikes a phosphor screen (P47), thereby creating the ion image, which is recorded by a charged-coupled device camera (SONY 1024×768 pixel, controlled using National Instruments (NI) LABVIEW 7.1 and IMAQ VISION software) and analyzed with a commercial software (DAVIS). The final image is obtained as the sum of around 40 000–100 000 laser shots depending on the quality of the signal.

Slice images of the CH_3^+ ions are recorded using a 500 ns extraction delay applied on the repeller plate and an effective 10 ns detector gate on the front MCP. The repeller voltage used is 5000 V and the detector voltages are 3.4 kV between back (output) MCP and phosphor screen and 1200 V between back and front (input) MCPs. The front MCP is gated using a pulse of 500 V. Ion images are recorded using two laser polarization geometries: X geometry (laser polarization parallel to the detector surface) and Z geometry (laser polarization perpendicular to the detector surface). Angular distri-

butions determined from the pump-and-probe XX images are normalized by the angular distributions measured in the corresponding ZX images, thus removing any systematic errors such as detector inhomogeneities.

III. THEORETICAL METHODOLOGY

A. Reduced dimensionality model

In order to describe the CH_3I system the reduced dimensionality model of Guo[35,37] has been used. In this model the CH_3I molecule is considered as a CXI pseudotriatomic molecule where the pseudoatom $X(X=H_3)$ is located at the center-of-mass (CM) of the three H atoms. The model considers three degrees of freedom (DOFs) represented by the (R,r,θ) Jacobi coordinates. The dissociation coordinate R is the distance between I and the CH_3 (or C–X) CM, r is the C–X distance, which represents the umbrella bend of the $C-H_3$ group (ν_2), and θ is the angle between the vectors associated with R and r, and it represents the X–C–I bend (ν_6). Modeling the umbrella mode of the $C-H_3$ group in CH_3I as a C–X stretch has been applied in various theoretical works, including both three[35,37,44,45] and two[11,36,40,41] dynamical DOFs, and they were able to reproduce successfully most of the experimental data. It has been discussed that the good description provided by the model is due to a large extent to the fact that dissociation occurs mainly along collinear configurations.

In the case of the 3D model applied in this work, the specific expression of the nuclear kinetic energy operator has been given in detail in a previous work.[2] Similarly, the constant and equilibrium values of the corresponding magnitudes used in the present calculations are also the same as those specified in Ref. 2.

B. Potential energy surfaces and initial state

The CH_3I photodissociation process in the A-band simulated here occurs upon optical excitation of the system from the $\tilde{X}\,{}^1A_1$ ground electronic state to the ${}^3Q_0$, ${}^1Q_1$, and ${}^3Q_1$ excited electronic states. Thus, four electronic potential energy surfaces are involved in the simulation of this process. The $\tilde{X}\,{}^1A_1$, ${}^1Q_1$, and ${}^3Q_1$ electronic surfaces correlate asymptotically with the $CH_3+I(^2P_{3/2})$ products, while the ${}^3Q_0$ surface correlates with the $CH_3+I^*(^2P_{1/2})$ products. In addition to the coupling of $\tilde{X}\,{}^1A_1$ to the three excited electronic states through electric-dipole moments, the ${}^3Q_0$ and ${}^1Q_1$ states are nonadiabatically coupled.

In order to model the four electronic potential energy surfaces we used available high-quality *ab initio* calculations of those surfaces. In the case of the $\tilde{X}\,{}^1A_1$ ground state, the potential surface is represented as a sum of three potential interactions in the R_{C-I} (the C–I nuclear distance), r, and θ coordinates, respectively. The interaction potential in the R_{C-I} coordinate is taken from the recently reported 2D ground-state potential for CH_3I, obtained by means of multireference SO configuration interaction *ab initio* calculations.[1,52] The potential interactions in the r and θ coordinates are modeled by harmonic oscillator functions. A detailed description of the $\tilde{X}\,{}^1A_1$ potential surface used has been given elsewhere.[2]

For the ${}^3Q_0$ and ${}^1Q_1$ excited electronic states and the nonadiabatic coupling between them, we used the *ab initio* surfaces calculated by Xie *et al.*,[45] which are an improved version of the previous nine-dimensional surfaces of Amatatsu *et al.*[43] The surfaces and nonadiabatic coupling of Refs. 43 and 45 have the same functional form, only differing in the value of some of the parameters used to fit the *ab initio* data, as a result of the larger basis set used in the *ab initio* calculations of Ref. 45. In order to reduce the dimensionality of the nine-dimensional surfaces, six out of the nine coordinates were fixed at their equilibrium values. Specifically, the three C–H distances were fixed to the value $r_1=r_2=r_3=2.05266a_0$, the angle ϕ between the plane containing the I–C bond and the plane containing one of the C–H bonds was fixed to 0°, and the three β angles (one of which is redundant) between the two planes containing C–H bonds were fixed to $\beta_1=\beta_2=\beta_3=120°$ (see Fig. 1 of Ref. 43). The resulting 3D surfaces are transformed to the (R,r,θ) Jacobi coordinates employed in the calculations.

Regarding the ${}^3Q_1$ state, the 2D *ab initio* potential energy surface of Alekseyev *et al.* has been used.[1,52] This 2D surface does not consider the dependence on the θ coordinate. In order to model the θ dependence of the ${}^3Q_1$ surface, it was assumed that such a dependence is the same as that of the ${}^1Q_1$ *ab initio* potential energy surface of Ref. 43. More specifically, the θ dependence of the ${}^1Q_1$ surface was fitted analytically assuming a fixed value of r (the r equilibrium value, r_e, in the CH_3-I interaction region) and varying R along the CH_3-I dissociation pathway. In this way an analytical function $f(r_e,R,\theta)$ is obtained which is added to the 2D ${}^3Q_1$ *ab initio* potential, providing the θ dependence of the surface along the dissociation coordinate R.

The electric-dipole moment functions $\mu_{ge}(R_{C-I})$ which couple radiatively the $\tilde{X}\,{}^1A_1$ ground state with the three excited electronic states were taken from the *ab initio* calculations of Alekseyev *et al.*[47,52] Actually, the *ab initio* $\mu_{ge}(R_{C-I})$ functions were fitted to analytical forms. In particular, the *ab initio* $\mu_{ge}(R_{C-I})$ function for the ${}^3Q_0 \leftarrow \tilde{X}\,{}^1A_1$ parallel transition was fitted to a straight line $\mu_{ge}(R_{C-I})=aR_{C-I}-b$, with $a=0.59$ Da_0^{-1} and $b=1.92$ D, in the R_{C-I} range where $\mu_{ge}(R_{C-I})\leq 1$ D, and this function was transformed to the (R,r,θ) Jacobi coordinates. For larger distances of the Jacobi R coordinate, the transition moment function $1.0/\{1.0+\exp[2.0(R-9.8)]\}$ suggested by Shapiro[11] was used. The *ab initio* $\mu_{ge}(R_{C-I})$ functions for the ${}^1Q_1 \leftarrow \tilde{X}\,{}^1A_1$ and ${}^3Q_1 \leftarrow \tilde{X}\,{}^1A_1$ perpendicular transitions were fitted to exponential functions $\mu_{ge}(R_{C-I})=A\exp[-\alpha(R_{C-I}-\bar{R}_{C-I})]$, with $A=0.47$ D, $\alpha=2.858a_0^{-1}$, and $\bar{R}_{C-I}=3.8a_0$ for the transition to ${}^1Q_1$ and $A=0.265$ D, $\alpha=2.91a_0^{-1}$, and $\bar{R}_{C-I}=3.8a_0$ for the transition to ${}^3Q_1$.

As we shall see below, there is evidence in the present experiments that excitation of CH_3I from $\tilde{X}\,{}^1A_1$ to the three excited electronic states takes place from vibrational states $v\geq 0$ of the C–I stretch mode, for the excitation wavelengths of current interest. Thus, dynamics simulations have been

carried out for initial states involving the ground vibrational state of CH_3I in the $\tilde{X}\ ^1A$ electronic state, and also involving the excitations $v=1-5$ of the C–I stretch vibration. All the above $\varphi_v^{J_iK_i}(R,r,\theta)$ initial states were calculated variationally using the Fourier grid Hamiltonian method,[53] with total angular momentum quantum numbers $J_i=0$ and $K_i=0$ (being K_i the projection of the total angular momentum J_i onto the body-fixed z axis). The procedure employed has been described in detail elsewhere.[2]

C. Wave packet dynamical simulations

A separate dynamical simulation is carried out for each $\varphi_v^{J_iK_i}(R,r,\theta)$ initial state ($v=0-5$). By exciting each $\varphi_v^{J_iK_i}(R,r,\theta)$ state to the three excited Q electronic states, a wave packet is prepared,

$$\Phi_v(R,r,\theta,\theta_R,\mathbf{Q},t=0) = \psi_{1,v}^{J|K|}(R,r,\theta,\theta_R,t=0)|1\rangle + \psi_{2,v}^{J|K|}(R,r,\theta,\theta_R,t=0)|2\rangle + \psi_{3,v}^{J|K|}(R,r,\theta,\theta_R,t=0)|3\rangle, \quad (1)$$

where $|1\rangle$, $|2\rangle$, and $|3\rangle$, denote the $^3Q_0$, $^1Q_1$, and $^3Q_1$ excited electronic states, respectively, $\mathbf{Q}$ denotes the electronic coordinates, and θ_R is the angle between the laser electric field polarization direction and the CH_3–I molecular axis R. For a parallel transition like $^3Q_0 \leftarrow \tilde{X}\ ^1A_1$ the values of J and K allowed are $J=J_i$ (forbidden if $K_i=0$), $J_i\pm1$, and $K=K_i$.[45,54,55] This means that since in our case $|J_iK_i\rangle=|00\rangle$, for $\psi_{1,v}^{J|K|}$ we have $J=1$ and $K=0$. For a perpendicular transition like $^1Q_1 \leftarrow \tilde{X}\ ^1A_1$ and $^3Q_1 \leftarrow \tilde{X}\ ^1A_1$, $J=J_i$, $J_i\pm1$, $K=K_i\pm1$.[45,54,55] Thus, for both $\psi_{2,v}^{J|K|}$ and $\psi_{3,v}^{J|K|}$ we have that $J=1$, $K=\pm1$, with the two components $K=1$ and $K=-1$ having equal weight in each packet $\psi_{2,v}^{11}$ and $\psi_{3,v}^{11}$. After some algebra one can determine that the specific expressions of the three initial packets are[54,55]

$$\psi_{1,v}^{10}(R,r,\theta,\theta_R,t=0) = \left(\frac{1}{8\pi^2}\right)^{1/2}\varphi_v^{00}(R,r,\theta)\mu_{01}(R,r,\theta)\cos\,\theta_R,$$

$$\psi_{2,v}^{11}(R,r,\theta,\theta_R,t=0) = -i\left(\frac{1}{8\pi^2}\right)^{1/2}\varphi_v^{00}(R,r,\theta)\mu_{02}(R,r,\theta)\sin\,\theta_R, \quad (2)$$

$$\psi_{3,v}^{11}(R,r,\theta,\theta_R,t=0) = -i\left(\frac{1}{8\pi^2}\right)^{1/2}\varphi_v^{00}(R,r,\theta)\mu_{03}(R,r,\theta)\sin\,\theta_R,$$

where μ_{01}, μ_{02}, and μ_{03} are the transition dipole moment functions coupling the ground state with the states $|1\rangle$, $|2\rangle$, and $|3\rangle$, respectively, and the initial packets exhibit the familiar $\cos\,\theta_R$ or $\sin\,\theta_R$ angular dependence for parallel and perpendicular transitions, respectively. In all of the simulations a grid consisting of a 15 point Gauss–Legendre quadrature has been used to represent the θ_R angle.

The experiments to be simulated were carried out using nanosecond laser pulses. The time scale of CH_3I photodissociation is much shorter, ~100–200 fs. Therefore we assumed in the simulations that the temporal profile of the nanosecond laser pulse does not vary significantly during the photodissociation process, and this profile was considered constant.

The time evolution of the amplitudes $\psi_{1,v}^{10}$, $\psi_{2,v}^{11}$, and $\psi_{3,v}^{11}$ is governed by a set of time-dependent coupled equations,

$$i\hbar\begin{pmatrix}\dot{\psi}_{1,v}^{10}\\ \dot{\psi}_{2,v}^{11}\\ \dot{\psi}_{3,v}^{11}\end{pmatrix} = \begin{pmatrix}\hat{H}_1 & \hat{V}_{12} & 0\\ \hat{V}_{21} & \hat{H}_2 & 0\\ 0 & 0 & \hat{H}_3\end{pmatrix}\begin{pmatrix}\psi_{1,v}^{10}\\ \psi_{2,v}^{11}\\ \psi_{3,v}^{11}\end{pmatrix}, \quad (3)$$

where $\hat{H}_i=\hat{T}+\hat{V}_i$ and $\hat{V}_{12}(\hat{V}_{12}=\hat{V}_{21})$ is the nonadiabatic coupling term between the $^3Q_0$ and $^1Q_1$ surfaces. In order to solve Eq. (3) the wave packet is represented in a basis set consisting of a 2D rectangular grid for the radial coordinates and an angular basis including 24 Legendre polynomials for the θ coordinate. The rectangular grid consists of 450 equidistant points in the R coordinate in the range $3.5a_0 \le R \le 16.0a_0$ and 32 equidistant points in the r coordinate in the range $-1.6a_0 \le r \le 1.6a_0$. Propagation of the wave packet is performed by representing the evolution operator by means of a Chebychev polynomial expansion. The wave packet was propagated for 200 fs with a time step $\Delta t=0.4$ fs. The wave packet is absorbed at the edge of the grid in the R coordinate after each propagation time step by multiplying each $\psi_{i,v}^{J|K|}$ packet by the function $\exp[-\alpha(R-R_{abs})^2]$, with $\alpha=0.9a_0^{-2}$ and $R_{abs}=13.0a_0$.

It is noted that the three wave packets of Eq. (3) to be propagated have total angular momentum $J=1$. In our simulations we treated this overall rotation in an approximate way using the centrifugal-sudden approximation. To this purpose we added to the $J=0$ Hamiltonians $\hat{H}_i$ of Eq. (3) the term $[J(J+1)-2K^2]/2\mu_R R^2$, with the appropriate J and K values for each $\psi_{i,v}^{J|K|}$ packet. We believe that this is a good approximation for such a low value as $J=1$.

We also note that the Hamiltonian matrix in Eq. (3) does not depend on the angle θ_R. Then one might think that it is enough to propagate $\psi_{i,v}^{J|K|}(R,r,\theta,t)$ packets without the θ_R dependence (either $\cos\,\theta_R$ or $\sin\,\theta_R$), which can be added to each $\psi_{i,v}^{J|K|}(R,r,\theta,t)$ packet at the end of the time propagation. This is not possible, however, due to the $\hat{V}_{12}$ nonadiabatic coupling term which mixes amplitude of the $\psi_{1,v}^{10}$ and $\psi_{2,v}^{11}$ packets, which have a different θ_R dependence [see Eq. (2)]. Thus, in this case, the calculation of photodissociation differential cross sections implies to transform a three nuclear DOF problem into an effective four DOF problem.

In order to obtain observable distributions of interest, the wave packet is projected out in the asymptotic region onto the states of the product fragments, namely, CH_3+I^* and CH_3+I. For these two dissociation channels the wave packet is projected out onto the rovibrational states of the C–X product (corresponding to the umbrella and bending modes) for the various excitation wavelengths probed in the experiment. Only the ground vibrational state $\nu=0$ of the umbrella mode is considered, since this is the vibrational state detected in the experiment. The projected out distributions are

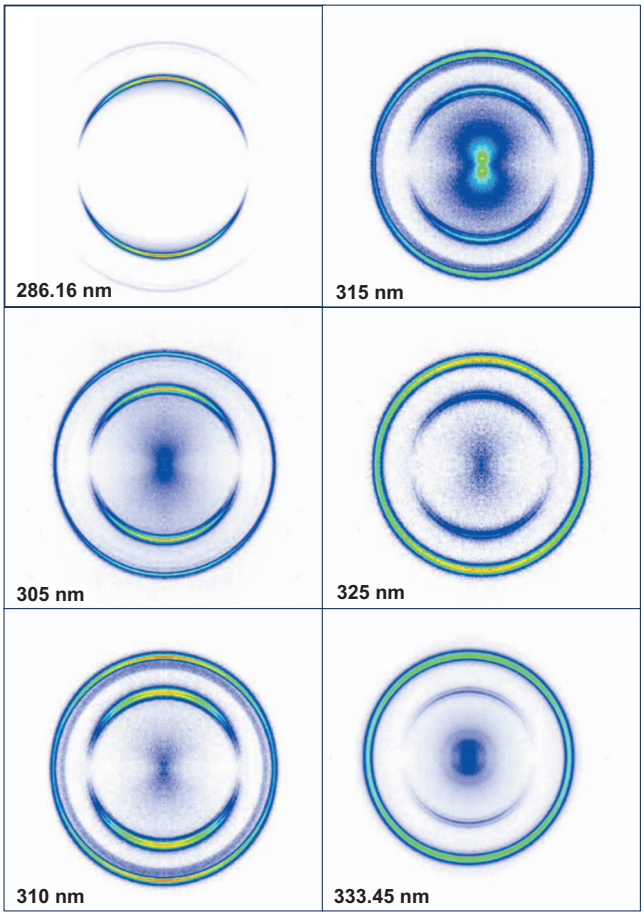

FIG. 1. Slice images of the $CH_3(\nu=0)$ ion fragment arising from the CH_3I photodissociation at different photolysis wavelengths in the red edge of the *A* absorption band in the range 286.16–333.45 nm. The different features observed in the images and their evolution with photolysis wavelength are commented on in the text.

obtained using the method of Balint-Kurti *et al.*[56,57] The procedure followed in our specific case has been described elsewhere.[2]

The final distributions of interest obtained from each simulation started by exciting a given $\varphi_v^{00}(R,r,\theta)$ initial state are weighted by a Maxwell–Boltzmann distribution $f(E_v,T)$ [being E_v the eigenenergy of the $\varphi_v^{00}(R,r,\theta)$ state and T the vibrational temperature] and then added together in order to obtain distributions comparable with the experimental ones. Unfortunately it is hard to estimate the vibrational temperature in the experiment, so actually T becomes a parameter of the theoretical model. We used $T=255$ K since we find that this value provides the best agreement between the experimental and theoretical results.

IV. EXPERIMENTAL RESULTS

A. Kinetic energy distributions

Figure 1 shows a series of sliced images corresponding to $CH_3(\nu=0)$ recorded for different photolysis laser wavelengths in the red tail region of the *A* absorption band of CH_3I between 286.15 and 333.45 nm. Three features can be distinguished in all the images: two more or less anisotropic rings corresponding to the formation of $CH_3(\nu=0)$ in correlation with I and I^* and a low-recoil anisotropic contribution which develops to a series of rings for the image taken at 333.45 nm.

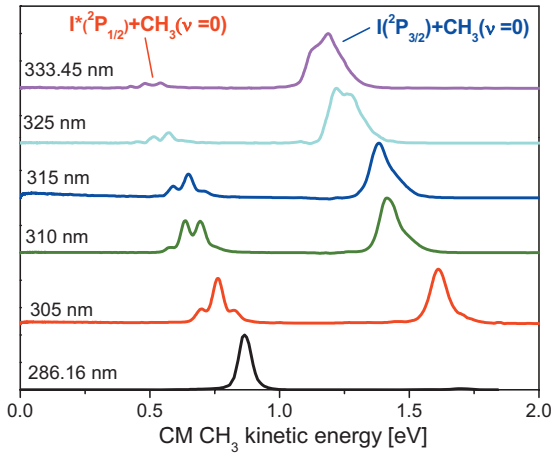

FIG. 2. CM $CH_3(\nu=0)$ kinetic energy distributions obtained by integration of the images shown in Fig. 1. The distributions are normalized arbitrarily to have the same overall intensity.

At the bluest photolysis wavelength 286.15 nm, the inner anisotropic ring, which corresponds to the $CH_3(\nu=0)+I^*$ channel, dominates the image while the outer anisotropic ring, associated with the $CH_3(\nu=0)+I$ channel, is barely visible. As we move photolysis wavelength toward the red tail of the absorption spectrum, the relative intensity of the $CH_3(\nu=0)+I$ channel increases, clearly surpassing that of the $CH_3(\nu=0)+I^*$ channel already at 310 nm, and widely dominating the image at 333.45 nm. To our knowledge, this is the first work to report a non-negligible contribution of the $CH_3(\nu=0)+I^*$ channel at 333.45 nm in an ion imaging experiment. We attribute this new result to the slice imaging technique, which is specifically suitable for this particular case: a nearly isotropic distribution, the $CH_3(\nu=0)+I$ channel, which buries a slower and much weaker inner feature, the $CH_3(\nu=0)+I^*$ channel. The usual and artificial inversion methods employed in velocity mapping are not able to clean the image with the accuracy necessary to observe the inner ring.

Integration of the images shown in Fig. 1 yields the kinetic energy distributions (KED) depicted in Fig. 2. Both in the images and the KED, a vibrational structure in the $CH_3(\nu=0)+I^*$ channel is clearly apparent. The structure is also visible in the images and KED for the $CH_3(\nu=0)+I$ channel, but with less resolution.

The energy balance for the photodissociation of CH_3I is given by

$$E_K = \frac{m_I}{m_{CH_3I}}[h\nu - D_0 + E_i(CH_3I) - E_{SO}[I(^2P_{j/2})], \qquad (4)$$

where E_K is the CM kinetic energy of the $CH_3(\nu=0)$ fragment, ν is the frequency of the photolysis laser, $D_0 = 2.41 \pm 0.03$ eV (Ref. 26) is the dissociation energy of the C–I bond, $E_{SO}[I(^2P_{j/2})]$ is the SO energy for the iodine atom in the ^2P state (for I, $E_{SO}=0$ and for I^*, $E_{SO}=0.943$ eV)[26] and $E_i(CH_3I)$ is the internal energy (rotation and vibration) of the parent molecule in the molecular beam. For a given

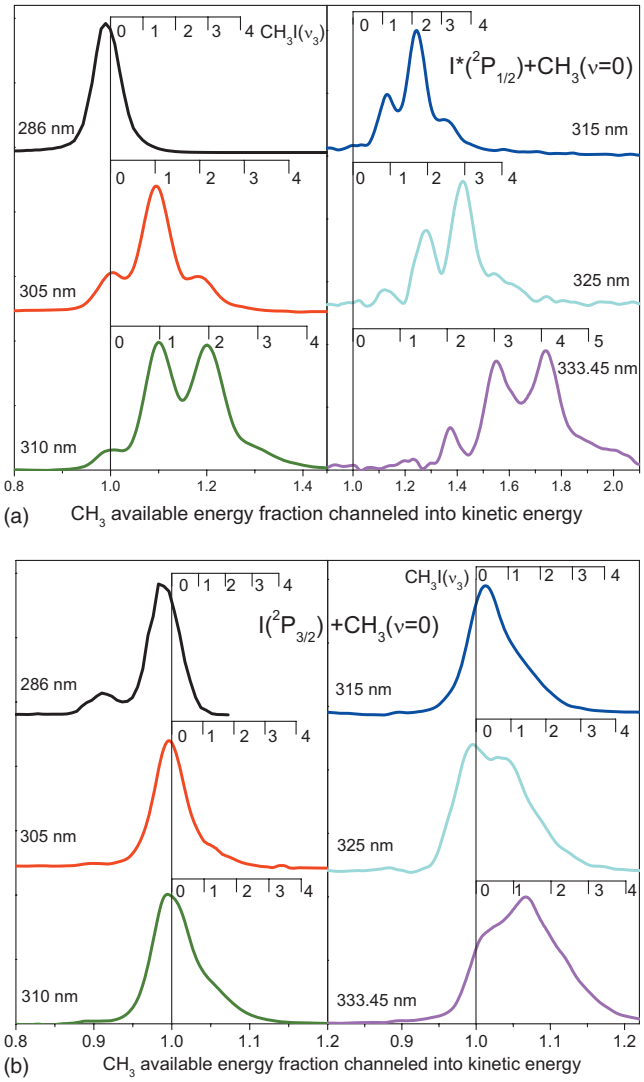

FIG. 3. Detailed kinetic energy distributions for the (a) $I^*+CH_3(\nu=0)$ and (b) $I+CH_3(\nu=0)$ product channels. In the abscissas, the $CH_3(\nu=0)$ fragment available energy fraction channeled into kinetic energy is represented. The combs in each panel correspond to the assignment of each peak in the kinetic energy distributions to ν_3 vibrational quantum states of the parent CH_3I molecule.

photolysis wavelength, the available energy for the methyl moiety is

$$E_{\mathrm{av}} = h\nu - D_0 - E_{\mathrm{SO}}[I(^2P_{j/2})] = E_K + E_i(\mathrm{CH_3I}). \quad (5)$$

The KED of the nascent $CH_3(\nu=0)$ normalized to the available energy for each photolysis wavelength is shown in Fig. 3. For each of the studied wavelengths, the distribution of the $CH_3(\nu=0)+I^*$ channel expands to energy values above E_{av} [see Fig. 3(a)], pointing out the contribution of vibrationally excited CH_3I to the overall process. A careful analysis of the well resolved structures appearing in Fig. 3(a) shows that the energy spacing is consistent with a vibrational quantum of 528 cm^{-1}, corresponding to the ν_3 (C–I stretching mode) vibration of the parent CH_3I.[27] The contribution of vibrationally hot CH_3I molecules changes noticeably with the photolysis wavelength. At 286.15 nm, most of the $CH_3(\nu=0)$ population in the $CH_3(\nu=0)+I^*$ channel comes from CH_3I in $\nu_3=0$. However, as photolysis wavelength increases, the contribution of $\nu_3>0$ increases. In particular, at 305 nm, the distribution peaks at CH_3I in $\nu_3=1$, and at 315 nm there is no appreciable input from vibrationally cold ($\nu_3=0$) parent molecule. At 333.45 nm the first contributory vibrationally excited state of CH_3I is $\nu_3=2$ and the maximum in the distribution corresponds to $\nu_3=4$.

Similar results at 305 nm were reported by Eppink and Parker[27] and attributed to photodissociation of vibrationally excited CH_3I. At room temperature the Boltzmann population of the ν_3 mode of CH_3I is only ≈8%. Experimentally, we work with the pulsed molecular beam in conditions to avoid the contribution of clusters by firing the laser pulses just at the very beginning of the gas pulse, where the vibrational cooling in the supersonic expansion is less efficient. This means that in these experimental conditions the population of vibrationally excited states of CH_3I in ν_3 although small is not negligible. At 305 nm, the present experimental results for the $CH_3(\nu=0)+I^*$ channel are very similar to those reported by Eppink and Parker using velocity mapping (see Fig. 10 in Ref. 27), where the maximum peak in the KED corresponds to $\nu_3=1$ with some contributions coming from CH_3I in $\nu_3=0$ and $\nu_3=2$. The clear appearance of these contributions from hot parent molecules at the reddest wavelengths is due to the enhanced Franck–Condon factors as we move to longer wavelengths[27] and has been successfully explained by the reflection absorption principle.[58]

The corresponding KED of the nascent $CH_3(\nu=0)$ normalized to the available energy for each photolysis wavelength for the $CH_3(\nu=0)+I$ channel is depicted in Fig. 3(b). As for the $CH_3(\nu=0)+I^*$ channel, the distributions expand to energy fractions above E_{av} as we move the photolysis wavelength to the red due to the increasing contribution of vibrationally excited CH_3I in ν_3. However, the effect is milder and the distributions are less resolved than for the $CH_3(\nu=0)+I^*$ channel. At the reddest photolysis wavelength studied (333.45 nm), the maximum peak corresponds to the contribution of CH_3I in $\nu_3=1$. In addition, a resolved peak is observed at an energy fraction of ≈0.9 (well below E_{av}), especially at 286.15 nm photolysis wavelength. This was attributed by Eppink and Parker[27] to activity of the ν_4 mode of the CH_3 fragment (the ν_4 mode has a fundamental frequency of 1396 cm^{-1}).[27]

An interesting observation from Figs. 3(a) and 3(b) is that at 333.45 nm photolysis wavelength, the ν_3 vibrational quantum numbers of the parent molecule contributing most to the observed $CH_3(\nu=0)$ product are $\nu_3=4$ and $\nu_3=1$ for the $CH_3(\nu=0)+I^*$ and $CH_3(\nu=0)+I$ channels, respectively. No $CH_3(\nu=0)$ correlating with I^* is seen from parent molecules in $\nu_3=0$ at this photolysis wavelength.

In order to check the effect of vibrational cooling in the supersonic expansion employed to produce the pulsed molecular beam and the possible contribution of parent molecule clusters photodissociation to the overall CH_3^+ signal, we scanned different regions of the pulsed molecular beam by changing the delay time between the laser and gas pulses. The results obtained for the one-laser experiment at 333.45 nm are shown in Fig. 4. In the top panel, we show three images taken at three different stages of the molecular beam and in the bottom panel the corresponding KED. Very early

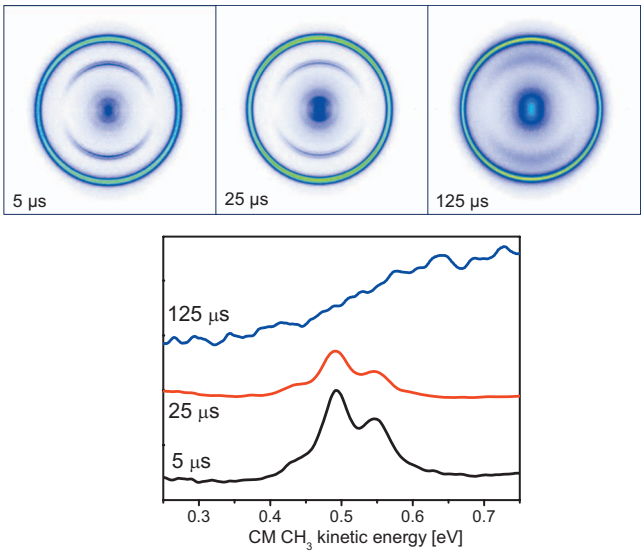

FIG. 4. Top: slice images of the $CH_3(\nu=0)$ ion fragment arising from the CH_3I photodissociation at 333.45 nm photolysis wavelength measured at different delay times between the laser and gas pulses in the range from 5 to 125 μs (see text for more details). Bottom: CM $CH_3(\nu=0)$ kinetic energy distributions corresponding to the slice images shown in the top panels.

in the expansion, in the first 5 μs, the vibrational cooling is poor and the $CH_3(\nu=0)+I^*$ channel displays a rich vibrational structure corresponding to $CH_3I(\nu_3>0)$. As the delay increases to 25 μs, the total intensity decreases, but the overall shape remains unmodified. It is around 120 μs later in the expansion when the parent species suffered enough number of collisions to relax to a larger extent its initial vibrational energy. As a consequence, this fact brings about the disappearance of the signal associated with the $CH_3(\nu=0)+I^*$ channel, which points toward a negligible absorption of CH_3I with $\nu_3<2$. In this part of the molecular beam some features related to cluster formation start to be observed.

The low-recoil anisotropic contribution in the images of Fig. 1 (especially that observed at 333.45 nm) can be attributed to dissociative ionization or photodissociation of the parent CH_3I^+ ion, as it has been observed before for CF_3I [59,60] and CH_3Br.[61,62] Aguirre and Pratt studied the two-photon resonant, three-photon ionization spectrum of CF_3I using velocity map imaging.[59,60] Two photon absorption in the wavelength interval ranging from 294 to 304 nm excites the parent molecule to a low energy Rydberg state, where it absorbs a third photon to reach the ionic ground state ($\tilde{X}\,^2E_{3/2}$). After the three photon absorption, the CF_3I^+ ion does not possess enough internal energy to dissociate and require absorption of an additional photon to decompose into $CH_3^+(\nu)$ and $I(^2P_{J/2})$ fragments. The well resolved structure appearing in the CF_3^+ images, weakly dependent on the excitation wavelength, was assigned to predissociation governed by the Franck–Condon factors between the CF_3 moiety in the CF_3I^+ and CF_3^+ fragment. Similar results have been published recently for the multiphoton photodissociation of CH_3Br.[61,62] Further slice imaging experiments are warranted to study the photodissociation of CH_3I^+ in more detail.

TABLE I. Anisotropy parameters β_2 and β_4 obtained from the images shown in Fig. 1 for the $CH_3(\nu=0)+I^*$ and $CH_3(\nu=0)+I$ channels. All contributions from different CH_3I initial vibrational states (ν_3) are included.

λ_{phot} (nm)	β_2	β_4
$CH_3(\nu=0)+I^*$ channel (all initial ν_3)		
286.16	2.63	0.80
305	2.17	0.32
310	2.12	0.28
315	2.00	0.22
325	1.72	0.20
333.45	1.51	0.27
$CH_3(\nu=0)+I$ channel (all initial ν_3)		
305	0.91	0.09
310	1.02	0.08
315	0.93	···
325	0.46	···
333.45	0.33	···

B. Angular distributions

The angular distributions for the $CH_3(\nu=0)+I$ and $CH_3(\nu=0)+I^*$ channels obtained integrating the experimental images of Fig. 1 have been fitted to the commonly used expression for one-photon dissociation and (2+1) REMPI detection processes:[63–66]

$$I(\theta)=\frac{\sigma}{4\pi}[1+\beta_2P_2(\cos\theta)+\beta_4P_4(\cos\theta)+\beta_6P_6(\cos\theta)], \quad (6)$$

where θ is the angle between the photofragment recoil direction and the photolysis polarization direction, σ is the absorption cross section (since the experimental setup has been not calibrated for total intensities, the quotient has been treated as a normalization fitting parameter), β_i are anisotropy parameters which reflect the dissociation dynamics and the photofragment polarization, and P_i are the Legendre polynomials of the order of i. If no photofragment polarization is expected, Eq. (6) can be truncated in $i=2$, and then, for this particular case, β_2 coincides with the anisotropy parameter, β.

Janssen *et al.*[67] demonstrated among others that the CH_3 fragment arising from the photodissociation of CH_3I in the A band has a propensity to inherit the K quantum number of the parent molecule. As a result, rotational alignment (v-j correlation) is observed. Although in the present experiments we have not carried out measurements at the necessary geometries to quantify the rotational alignment of the CH_3 fragment, we used Eq. (6) to fit our angular distributions.

The anisotropy parameters obtained from the fitting when considering all the contributions from the different CH_3I ν_3 vibrational states (i.e., angular distributions obtained by integration of the whole ring in the image independently of the observed structure) are summarized in Table I. In the fitting procedure only the β_2 and β_4 parameters are needed. For the $CH_3(\nu=0)+I^*$ channel, the β_2 parameter decreases monotonically, while the β_4 parameter takes a nearly constant value of $\approx$0.20–0.27 for photolysis wavelengths in the

red tail of the A absorption band (see Table I). The $CH_3(\nu=0)+I^*$ products arise from a parallel absorption to the $^3Q_0$ state followed by adiabatic dissociation. The dynamics is not supposed to change in the studied photolysis wavelength range and an anisotropic parameter $\beta=2$ can be assumed in all cases. The variations in β_2 and β_4 can be assigned to the dependence of the rotational alignment of the $CH_3(\nu=0)$ radical on the photolysis wavelength for this channel.

For the $CH_3(\nu=0)+I$ channel, the value of β_4 is almost negligible, being in fact zero for the largest wavelengths. In this case, β_2 nearly represents the anisotropy of the photodissociation process. The values for β_2 presented in Table I change substantially with the photolysis wavelength, taking an approximately constant value close to 1 for wavelengths above 315 nm, and decreasing values as low as 0.33 at 333.45 nm. The deviation from the value of $\beta=2$ for a parallel transition, which becomes larger as we move to larger photolysis wavelengths, is a measure of the increasing participation of the $^3Q_1$ potential surface (perpendicular transition) in the dynamics yielding $CH_3(\nu=0)+I$ products. A careful inspection of the images shows that the ring structure of the $CH_3(\nu=0)+I$ channel attributed to the participation of different initial $CH_3I(\nu_3)$ vibrational states displays a distinct anisotropy behavior. At the poles of the images the ring is broader than at the equator, in such a way that the contribution of $CH_3I(\nu_3>0)$ appears more substantially in the poles. Therefore, the parallel contribution in the ring is associated with high vibrational states of the CH_3I, whereas low vibrational states contribute more to the perpendicular contribution. Interestingly, in Ref. 27 the opposite effect was reported at the photolysis wavelength of 305 nm; that is, the ring is broader at the equator of the images, which the authors assign to an anisotropic contribution of $CH_3I(\nu_6=1)$. Nevertheless, in Ref. 27, such effect is only apparent in the raw images.

In order to study this initial vibrational state dependence of the anisotropy, the signal of the ring for the $CH_3(\nu=0)+I$ channel associated with the different initial vibrational states of CH_3I is integrated separately. Although the overlapping between the contributions from the different vibrational states in the KED does not allow a total independent analysis [see Fig. 3(b)], it is possible to separate to some extent the behavior of $\nu_3=0$ from that of the excited levels ($\nu_3>0$). To do that, we integrated separately the "left part" of the KEDs shown in Fig. 3(b) (where the main contribution is from $\nu_3=0$) and the "right part" (where it should not have a significant contribution from $\nu_3=0$). The "left" and "right" parts have been selected in each case. The results are presented in Table II and the angular distributions for three particular photolysis wavelengths (310, 325, and 333.45 nm) are shown in Fig. 5. The main result that stands out is the change in anisotropy for $\nu_3>0$ as photolysis wavelength increases. While for $\nu_3=0$, β_2 and β_4 take almost constant values corresponding to a parallel transition, for $\nu_3>0$, the anisotropy changes from a parallel-type distribution toward a perpendicular-type distribution. These results are discussed below in the light of the theoretical results that will be presented in next section.

TABLE II. Anisotropy parameters β_2 and β_4 obtained from the images shown in Fig. 1 for the $CH_3(\nu=0)+I$ channel. (a) Integration of the "inner" part of the ring, corresponding to $CH_3I(\nu_3\approx0)$. (b) Integration of the "outer" part of the ring, corresponding to $CH_3I(\nu_3>0)$. See text for details.

λ_{phot} (nm)	β_2	β_4
	(a) $CH_3(\nu=0)+I$ channel, $CH_3I(\nu_3\approx0)$	
305.0	1.63	0.16
310.0	1.68	0.29
315.0	1.97	0.34
325.0	1.35	···
333.45	1.15	···
	(b) $CH_3(\nu=0)+I$ channel, $CH_3I(\nu_3>0)$	
305.0	0.47	···
310.0	0.48	−0.08
315.0	0.44	−0.04
325.0	−0.30	···
333.45	−0.41	0.18

V. THEORETICAL RESULTS

A. Kinetic energy distributions

Figure 6 shows the radial distributions in the R coordinate associated with the initial $\psi_{i,v}^{J|K|}$ packets of Eq. (2) (which are obtained by integrating the square of the $\psi_{i,v}^{J|K|}$ packets over the r, θ, and θ_R variables). Such distributions reflect the shape along the R coordinate of the $\varphi_v^{00}(R,r,\theta)\mu_{0i}(R,r,\theta)$ packets prepared initially on the three i excited electronic potential surfaces. As expected, as v increases the $\psi_{i,v}^{J|K|}$ initial packet span an increasingly larger range of R, both at short and long distances. The area of the different radial distributions is not normalized to unity, and it increases with increasing v. This is a reflection of the fact that whereas the $\varphi_v^{00}(R,r,\theta)$ packets are normalized to unity, the $\varphi_v^{00}(R,r,\theta)\mu_{0i}(R,r,\theta)$ products are not, and the area of the corresponding R distribution increases with v due to the in-

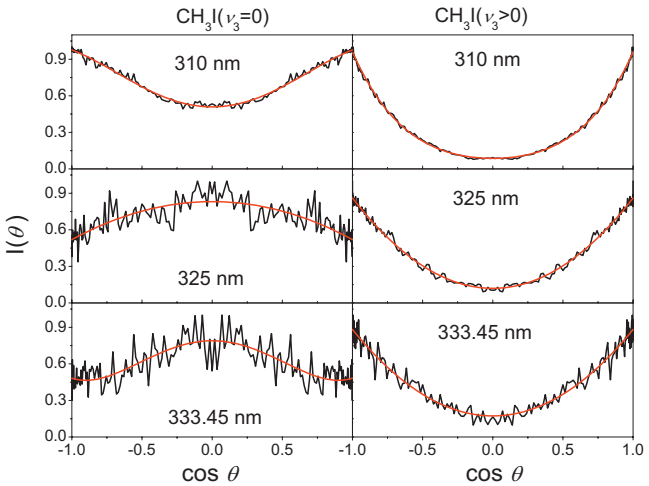

FIG. 5. $CH_3(\nu=0)$ angular distributions at different photolysis wavelengths as indicated obtained by integrating the outer ring of the slice images shown in Fig. 1. Left panels: integration of the outer part of the ring, which corresponds to the photodissociation of $CH_3I(\nu_3>0)$. Right panels: integration of the inner part of the ring, which corresponds to the photodissociation of $CH_3I(\nu_3\approx0)$. Black curves: experimental data. Red curves: fit to Eq. (6). The fit parameters are listed in Tables I and II.

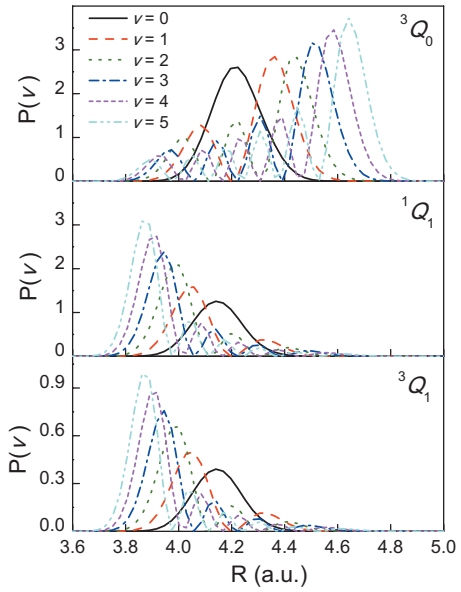

FIG. 6. Radial distributions along the dissociation coordinate R associated with the $\psi_{i,v}^{|K|}$ wave packets initially prepared in the $^3Q_0$, $^1Q_1$, and $^3Q_1$ excited electronic states.

creasing spreading of $\varphi_v^{00}(R,r,\theta)$ along R. The distributions of Fig. 6 reflect also the shape of the μ_{0i} functions along R, namely, an increasing function with increasing R for the $^3Q_0 \leftarrow \tilde{X}\ ^1A_1$ transition (maximizing the distribution intensity at large R), and a decreasing function with increasing R for the $^1Q_1 \leftarrow \tilde{X}\ ^1A_1$ and $^3Q_1 \leftarrow \tilde{X}\ ^1A_1$ transitions (maximizing the distribution intensity at short R).[47] These radial distributions will be useful to interpret the absorption spectra for the different initial vibrational states v discussed below.

Kinetic energy distributions of the $CH_3(\nu=0)$ fragment for the $CH_3(\nu=0)+I^*$ and $CH_3(\nu=0)+I$ channels were calculated for the photolysis wavelengths 286.16, 305, 310, 315, 325 and 333.45 nm, and they are shown in Fig. 7. These KEDs have been weighted using a Maxwell–Boltzmann distribution $f(E_v,T)$ with $T=255$ K (see Sec. III C). The calculated distributions display two main trends. The first trend is that vibrational excitation of the C–I stretch mode increases

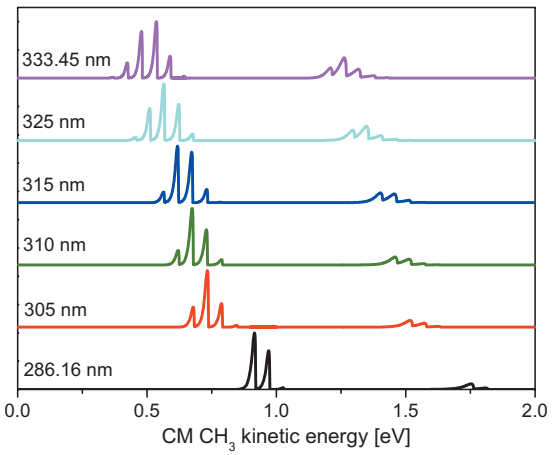

FIG. 7. Theoretical CM $CH_3(\nu=0)$ kinetic energy distributions for the $CH_3(\nu=0)+I^*(I)$ products produced upon photodissociation with different photolysis wavelengths.

substantially with increasing excitation wavelength. This trend is found for the two dissociation channels producing I^* and I fragments, and it agrees with the trend found in the distributions measured experimentally (see Figs. 2 and 3). Vibrational excitation increases more slowly in the case of photodissociation into $CH_3(\nu=0)+I$, also in agreement with experiment. For all of the excitation wavelengths the peaks associated with the different initial vibrational states v are broader in the dissociation channel leading to I fragments, indicating that the corresponding $CH_3(\nu=0)$ fragments are rotationally more excited than those produced through the $CH_3(\nu=0)+I^*$ channel.

The second trend exhibited by the distributions of Fig. 7 is that the intensity associated with the $CH_3(\nu=0)+I$ product fragments increases with increasing excitation wavelength. Again this behavior is also found in the experimental kinetic energy distributions. However, this increase in intensity is very much underestimated in the theoretical results. Indeed, in the theoretical distributions, the intensity of the I dissociation channel remains lower than that of the I^* channel for all the wavelengths studied, while the experimental data show that the I channel becomes dominant for photolysis wavelengths ≥ 305 nm.

The intensity associated with the $CH_3(\nu=0)+I^*$ products in the kinetic energy distributions comes only from dissociation in the $^3Q_0$ electronic potential surface. However, the intensity obtained for the $CH_3(\nu=0)+I$ product channel comes from dissociation in two different electronic surfaces, $^1Q_1$ and $^3Q_1$. In addition, the final intensity found in the $^1Q_1$ surface is the sum of the population initially excited to this surface plus the population transferred from the $^3Q_0$ state through the nonadiabatic coupling. It is therefore interesting to analyze how these different contributions to the intensity of the I product channel change with the excitation wavelength, since it provides valuable information on how the photodissociation process takes place. Thus, the intensities projected out of the $\psi_{2,v}^{11}$ and $\psi_{3,v}^{11}$ packets evolving on the $^1Q_1$ and $^3Q_1$ surfaces, respectively, have been analyzed and they are shown in Fig. 8 along with the total intensity of the I product channel for the different wavelengths.

The main result of Fig. 8 is that the contribution of dissociation in the $^3Q_1$ electronic surface to the I product channel intensity increases rapidly with increasing photolysis wavelength. Actually, the $^3Q_1$ contribution becomes dominant for $\lambda_{phot} \geq 310.0$ nm. This result indicates a substantial increase in the cross section of absorption to the $^3Q_1$ state as λ_{phot} increases. Although the increase in the $^3Q_1$ contribution to the intensity occurs for all of the initial vibrational states, it is particularly remarkable and faster for the lowest $v=0$ and $v=1$ states.

Regarding the $^1Q_1$ contribution to the distributions of Fig. 8, it is not possible to separate, and therefore to discern quantitatively, the amount of intensity coming from $^3Q_0$ through nonadiabatic transition from that initially excited to $^1Q_1$. However, some qualitative information on this point can be obtained from magnitudes like the absorption spectra, as shown below.

The peaks associated with the initial vibrational states in the kinetic energy distributions shown in Fig. 7 have been

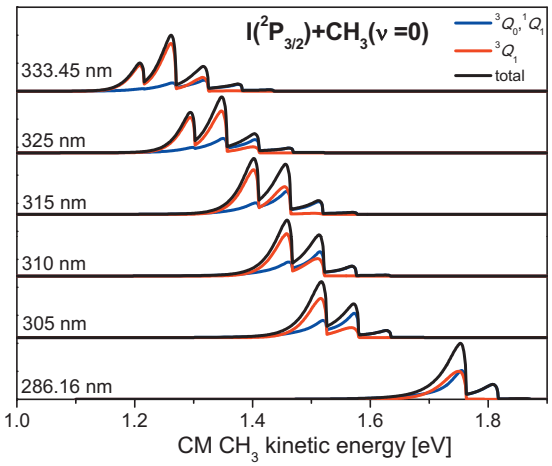

FIG. 8. Theoretical CM $CH_3(\nu=0)$ kinetic energy distributions for the $CH_3(\nu=0)+I$ channel produced upon photodissociation with different photolysis wavelengths. The figure shows the total intensity (which is the same as that shown in Fig. 7) and the separated contributions to this intensity produced by photodissociation from the $^3Q_0/^1Q_1$ and $^3Q_1$ electronic states.

fitted to a Maxwell–Boltzmann distribution $f(E_j^{(\nu=0)}, T_{\rm rot})$, where $E_j^{(\nu=0)}$ are the rotational eigenenergies of the $CH_3(\nu=0)$ fragment. From these fits the rotational temperatures $T_{\rm rot}$ associated with all the peaks are obtained. Rotational temperatures have been obtained for the I^* and I product channels and, in addition, for the I channel temperatures have also been estimated for the peaks corresponding to the $^1Q_1$ and $^3Q_1$ contributions (see Fig. 8). Rotational temperatures were estimated only for the peaks of Figs. 7 and 8 with a non-negligible intensity, and are collected in Table III.

The rotational temperatures found for the $CH_3(\nu=0)+I^*$ product channel are much lower than those of the $CH_3(\nu=0)+I$ channel, in agreement with previous experiments. This is expected, since there is more energy available for the $CH_3(\nu=0)+I$ products (almost 1 eV corresponding to the excitation energy of the I^*), which produces rotationally hotter $CH_3(\nu=0)$ fragments, as mentioned above. The broader rotational distributions of the $CH_3(\nu=0)$ products in the $CH_3(\nu=0)+I$ channel imply a larger overlap between the peaks in the KED corresponding to the different initial v states of CH_3I, which explains the lower vibrational resolution in the KED found for the I product channel. A decreasing amount of energy available for the fragments also explains that for both the I^* and I product channels the temperatures typically decrease with increasing photolysis wavelength.

For the I^* product channel the rotational temperature typically decreases as v increases for each photolysis wavelength, although the change in temperature is not large. This behavior is rather unexpected, since in terms of energy avail-

TABLE III. Rotational temperatures calculated by fitting the peaks with appreciable intensity associated with different v states of the KEDs of Figs. 7 and 8 to a Maxwell–Boltzmann distribution. Errors range from $<\pm 5$ to ± 40 K.

$\lambda_{\rm phot}$ (nm)	$v=0$	$v=1$	$v=2$	$v=3$	$v=4$	$v=5$
			I^* product channel, $T_{\rm rot}$/K			
286.16	145	135	115			
305.0	140	138	135	115		
310.0	135	132	127	120	115	
315.0	128	126	125	120	105	
325.0	115	113	113	113	108	108
333.45	105	105	110	110	108	108
			I product channel, $T_{\rm rot}$/K			
286.16	430	500	590			
305.0	330	460	530	700		
310.0	300	420	510	640	730	
315.0	290	360	500	610	830	
325.0	260	300	400	530	700	800
333.45	250	265	320	450	610	860
			I product channel, $^1Q_1$ contribution, $T_{\rm rot}$/K			
286.16	450	500	620			
305.0	430	470	530	720		
310.0	430	460	510	650	710	
315.0	410	450	500	620	810	
325.0	330	400	470	560	730	770
333.45	320	390	470	550	720	760
			I product channel, $^3Q_1$ contribution, $T_{\rm rot}$/K			
286.16	370					
305.0	300	320				
310.0	280	300				
315.0	270	280	330			
325.0	250	270	280			
333.45	240	260	280			

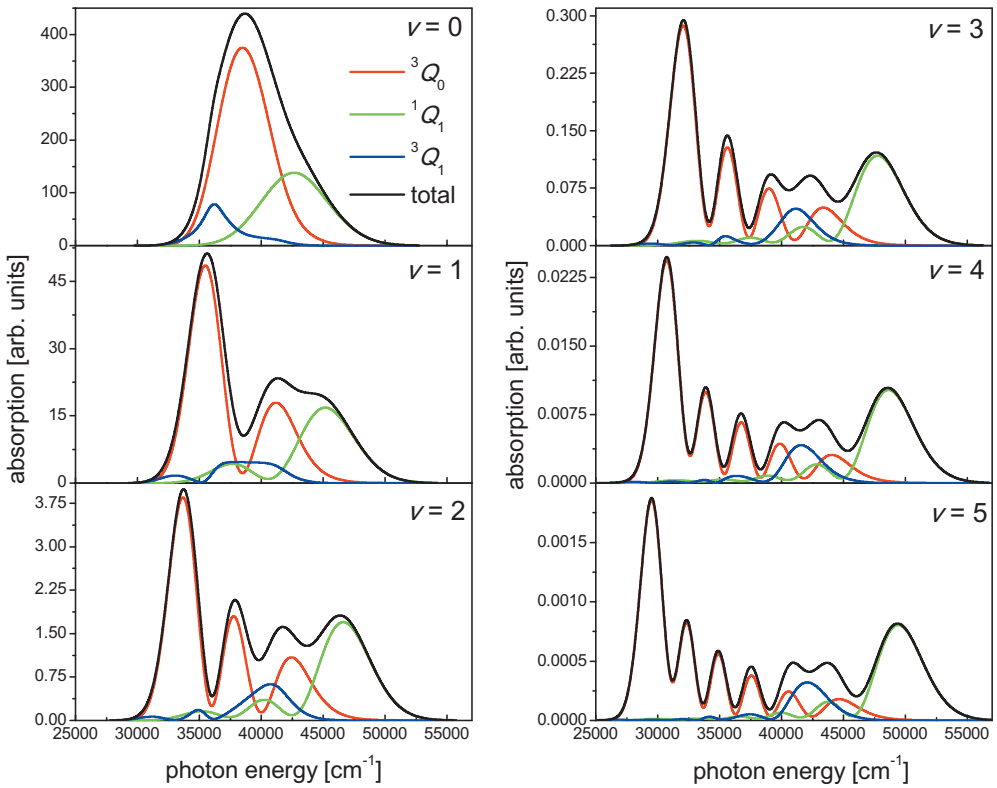

FIG. 9. Theoretical absorption spectra for the six $v=0-5$ vibrational states of the parent CH_3I molecule. Each panel shows the total absorption spectrum and the spectra associated with the $^3Q_0$, $^1Q_1$, and $^3Q_1$ excited electronic states.

able one would expect the opposite trend. Indeed, as v increases a higher excitation energy is reached with a given photon wavelength, which leaves an increasingly larger amount of energy available for the fragments. Therefore, an increase in the rotational temperature with v would be expected. The opposite behavior found may indicate that mechanisms of energy transfer from rotation to translation occur to some extent in the I^* product channel as v increases.

In the I product channel, on the contrary, the rotational temperature typically increases with increasing v. In addition, the increase in the temperature is very remarkable, larger than that expected from a rise of available energy when higher v states are excited. Analysis of the rotational temperatures associated with the $^1Q_1$ and $^3Q_1$ contributions to the I product channel helps understand this behavior. It is found that the rotational temperatures of the $^3Q_1$ peaks rise slightly with increasing v. This rise in temperature is consistent with a larger energy available as vibrational excitation increases. However, the corresponding increase in rotational temperatures of the $^1Q_1$ peaks is clearly faster, and in fact it is what causes the overall fast rise of temperatures with increasing v of the I product channel. As will be discussed next in Sec. V B, the $^1Q_1$ intensity of the I product channel comes mainly from the $^3Q_0$ electronic state through nonadiabatic transitions. It thus suggests that the nonadiabatic transition may induce a mechanism of energy transfer from translation to rotation, which becomes more intense as v increases. An interesting question arises about whether the energy transfer mechanisms between fragment rotation and translation modes, occurring in opposite directions for the wave packet amplitude remaining in the $^3Q_0$ state (and giving rise to the I^* product channel intensity) and for the wave packet amplitude nonadiabatically transferred from $^3Q_0$ to $^1Q_1$, are related.

B. Absorption spectra

It is helpful and illustrating to analyze the absorption spectra associated with each initial vibrational state v excited in order to unravel several aspects of the CH_3I photodissociation dynamics in the present range of photolysis wavelengths. Such spectra are displayed in Fig. 9 for $v=0-5$ along with the separated spectral components associated with the three absorbing excited electronic states $^3Q_0$, $^1Q_1$, and $^3Q_1$. The shape of the $^3Q_0$, $^1Q_1$, and $^3Q_1$ components of each v absorption spectrum resembles the shape of the corresponding radial distributions of Fig. 6, as expected from the reflection principle.[68] Differences between the present absorption spectra and those obtained in Ref. 47 for $v=0$, 1, and 2 are attributed mainly to the fact that the present 3D treatment considers the CH_3I bending mode, while the 2D treatment of Ref. 47 does not. The spectra of Fig. 9 are weighted with the same Maxwell–Boltzmann distribution $f(E_v,T)$ with $T=255$ K (see Sec. III C) used to weight the kinetic energy distributions of Figs. 7 and 8. This explains the decreasing absorption intensity of the spectra as v increases. The range of photon energies relevant to the present study goes from nearly 30 000 cm^{-1} for $\lambda=333.45$ nm to $\sim$35 000 cm^{-1} for $\lambda=286.16$ nm.

As commented above in this section, the probability of getting $CH_3(\nu=0)+I$ fragments found in the $^1Q_1$ electronic state potential surface is a mixture of wave packet intensity

initially excited to the $^1Q_1$ state and wave packet intensity transferred from $^3Q_0$ through the nonadiabatic coupling. Although these two contributions cannot be separated, the spectra of Fig. 9 give information on the amount of each of them. Indeed, Fig. 9 shows that in the energy range 30 000–35 000 cm^{-1} the $^3Q_0$ absorption cross section is far higher than the $^1Q_1$ one, although only a fraction of this $^3Q_0$ absorption intensity will undergo a nonadiabatic transition to $^1Q_1$. Calculations of I^* yields in wave packet dynamics simulations considering only the $^3Q_0$ and $^1Q_1$ excited electronic states and assuming initial excitation only to $^3Q_0$ find that for $\lambda_{phot} > 286$ nm the probability of $^1Q_1 \leftarrow {}^3Q_0$ nonadiabatic transitions is >15% (see Fig. 12 of Ref. 37). With this estimate of the probability of $^1Q_1 \leftarrow {}^3Q_0$ nonadiabatic transition and the large absorption intensities to $^3Q_0$ found in the spectra in the relevant energy region, the implication is that the dominant contribution to the probability of $CH_3(\nu=0)+I$ products found in the $^1Q_1$ electronic state comes from the $^1Q_1 \leftarrow {}^3Q_0$ nonadiabatic transition instead from population initially excited to the $^1Q_1$ state.

The absorption spectra of Fig. 9 also explain why for shorter photolysis wavelengths, like 266 nm, only the initial $v=0$ vibrational state contributes to the reaction (as found experimentally), while as λ_{phot} increases the contribution from initial vibrational excited states increases as well, as found in this work both experimentally and theoretically. The photon energy corresponding to $\lambda_{phot}=266$ nm is ~37600 cm^{-1}. At this energy (and in the nearby region of energies), the absorption intensities for $v>0$ are very small or negligible as compared to that of $v=0$, which explains that only $v=0$ is excited and contributes with appreciable intensity. This result is produced by the combination of the specific shape of the v absorption spectra and (mainly) the fact that the initial population of the vibrational states v before excitation decays very fast with increasing v.

When λ_{phot} increases and the photon energy decreases, the absorption intensity for $v=0$ decays fast. In the spectra of $v>0$ what happens is that as v increases the main peak of the spectra shifts gradually toward lower photon energies. This is a consequence of the increasing size of the R range (particularly at long R distances) spanned by the vibrational state initially excited as v increases (see Fig. 6). The effect is that as the photon energy decreases, the absorption intensity due to $v>0$ becomes comparable and even higher than the $v=0$ absorption intensity. The increasing absorption intensity of the $v>0$ states explains the increasing contribution of initial vibrational excited states found in both the experimental and theoretical kinetic energy distributions with increasing λ_{phot}.

The absorption spectra also explain the fast increase in the $^3Q_1$ contribution to the probability of $CH_3(\nu=0)+I$ products found in the distributions of Fig. 8. The spectra corresponding to $v=0$ and 1 show that, as the photon energy decreases in the range 30 000–35 000 cm^{-1}, the intensity of the $^3Q_1$ component becomes comparable to the $^3Q_0$ intensity and even overcomes it. This causes the fast increase in the $^3Q_1$ intensity found for $v=0$ and 1 in the translational energy distributions of Fig. 8. The $^3Q_1$ intensity due to $v=0$ and 1 becomes the dominant contribution to the translational energy distributions of the I product channel for $\lambda_{phot} \geq 310$ nm, i.e., for photon energies $\leq 32\,300$ cm^{-1}, which is consistent with the $^3Q_1/{}^3Q_0$ ratio of absorption intensities displayed by the $v=0$ and 1 spectra in that energy range. For $v>1$ the spectra of Fig. 9 show that the $^3Q_1/{}^3Q_0$ ratio of absorption intensities increases much more slowly with decreasing photon energy, which explains the much slower increase in the $^3Q_1$ contribution due to $v>1$ to the total intensity of the distributions of Fig. 8. The above discussion also explains the experimental and theoretical finding that vibrational excitation in the $CH_3(\nu=0)+I$ channel KED is significantly lower (essentially reduced to $v=0$ and 1 contributions) than in the $CH_3(\nu=0)+I^*$ channel

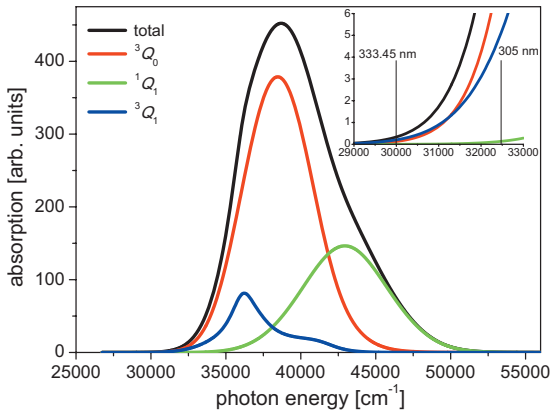

FIG. 10. Total absorption spectrum obtained by summing the six partial spectra corresponding to each initial vibrational state v shown in Fig. 9. The figure also shows the spectral components associated with the $^3Q_0$, $^1Q_1$, and $^3Q_1$ excited electronic states. The inset is a magnification of the region corresponding to the absorption wavelengths in the range 305–333.45 nm.

By summing the six Maxwell–Boltzmann-weighted spectra of Fig. 9 we obtained a total absorption spectrum, which includes the contribution of all the initial vibrational states involved in the photodissociation process (see Fig. 10). This is the absorption spectrum associated with the total wave packet prepared by the excitation to $^3Q_0$, $^1Q_1$, and $^3Q_1$ when CH_3I is initially in $\tilde{X}\,{}^1A_1$ at a vibrational temperature $T=255$ K. As expected, the shape of this spectrum is actually very similar to that of the $v=0$ spectrum, which is the main contribution. The contribution of $v=1$ is the only appreciable one in addition to that of $v=0$. The $v=1$ contribution has the effect of changing the spectrum of Fig. 10 with respect to the $v=0$ spectrum in the 30 000–35 000 cm^{-1} range of interest. This change involves an increase in the intensity of absorption to $^3Q_0$ compared to the $^3Q_1$ absorption intensity.

C. Angular distributions

Angular distributions were calculated for photodissociation into the $CH_3(\nu=0)+I^*$ and $CH_3(\nu=0)+I$ product channels. In the case of the I product channel separate angular distributions were calculated for the contributions coming from the $^1Q_1$ and $^3Q_1$ electronic states. Typical distributions for each electronic state are shown in Fig. 11. The angular distributions obtained for $^3Q_0$ and $^3Q_1$ display the expected shape for distributions associated with a parallel and a per-

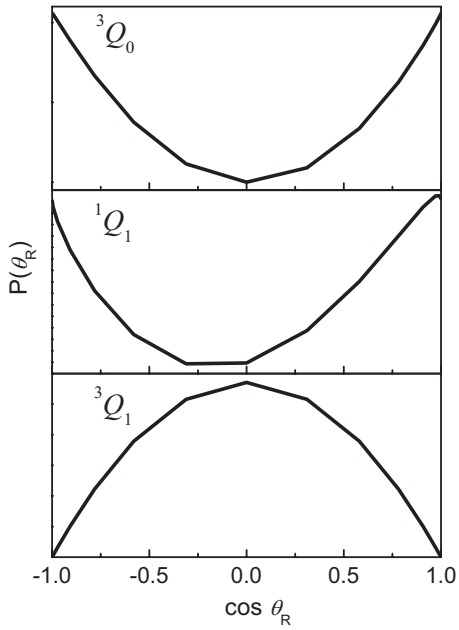

FIG. 11. Theoretical angular distributions obtained on the $^3Q_0$ (for λ_{phot} =333.45 nm), $^1Q_1$ (for λ_{phot}=305.0 nm), and $^3Q_1$ (for λ_{phot}=310.0 nm) excited electronic states.

pendicular transition, respectively. Correspondingly, when these distributions are fitted to the familiar expression,[63]

$$\frac{d\sigma}{d\Omega}(\theta_R) = \frac{\sigma}{4\pi}[1 + \beta P_2(\cos\theta_R)], \tag{7}$$

where σ is the integral cross section, β is the anisotropy parameter, and $P_2(\cos\theta_R)$ is the second order Legendre polynomial, the values of β obtained are β=2 for the $^3Q_0$ distributions and β=−1 for the $^3Q_1$ distributions for all the photolysis wavelengths.

More surprising is the behavior of the angular distributions obtained for the $^1Q_1$ electronic state. They are typically nonsymmetric with respect to θ_R=90° (see middle panel of Fig. 11). The reason of this asymmetry is the following. In the asymptotic region, the packet in the $^1Q_1$ electronic state can be expressed as $\psi^{11}_{2,v}(R,r,\theta,\theta_R,t)=\xi_{2,v}(R,r,\theta,t)\cos\theta_R + \eta_{2,v}(R,r,\theta,t)\sin\theta_R$, where $\xi_{2,v}$ is the wave packet amplitude transferred from $^3Q_0$ to $^1Q_1$ through the nonadiabatic coupling, and $\eta_{2,v}$ is the amplitude initially excited in the optical transition $^1Q_1 \leftarrow \tilde{X}\ ^1A_1$. Let us denote by a and b (which are complex quantities) the sum of the amplitudes projected out asymptotically of the $\xi_{2,v}$ and $\eta_{2,v}$ packets, respectively, onto the $CH_3(\nu=0)$+I product fragment states. Thus, the total amplitude projected out of the $\psi^{11}_{2,v}$ packet is $a\cos\theta_R + b\sin\theta_R$, and its square $|a|^2\cos^2\theta_R + |b|^2\sin^2\theta_R + (ab^* + a^*b)\cos\theta_R\sin\theta_R$ is what causes the asymmetry of the $^1Q_1$ angular distributions.

If the b amplitude is very small compared to a, the asymmetry $(ab^*+a^*b)\cos\theta_R\sin\theta_R$ term becomes negligible. However, if b (which is expected to be smaller than a, as discussed above) has a non-negligible value compared to a, the $(ab^*+a^*b)\cos\theta_R\sin\theta_R$ term will cause an appreciable manifestation of asymmetry in the angular distribution. This is actually what happens for the photolysis wavelengths

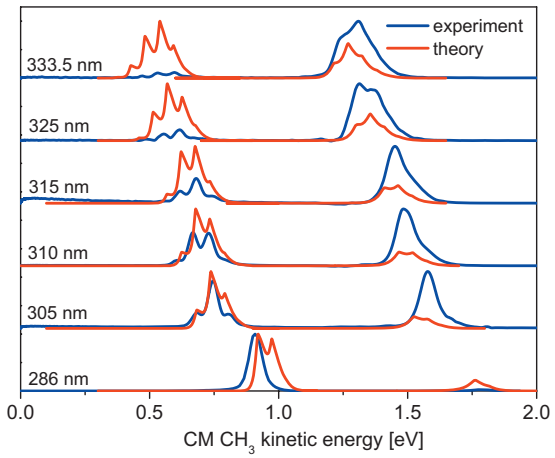

FIG. 12. Comparison between the experimental and theoretical kinetic energy distributions. The theoretical curves have been convoluted with a Gaussian function modeling the experimental resolution. See text for details.

λ_{phot}=286.16, 305, 310, and 315 nm, and the explanation can be found in the absorption spectra corresponding to v=1 and 2 of Fig. 9. Indeed, in the energy range of the above photolysis wavelengths the intensity of absorption to $^1Q_1$ is quite significant for v=1 and 2, which are typically the main contributions to the $^1Q_1$ angular distributions, as shown by the distributions of Fig. 8. As a result, these asymmetric angular distributions cannot be fitted to the expression of Eq. (7) in order to obtain a value of the β parameter. Manifestations of asymmetry in the angular distributions are smaller for λ_{phot} =325.0 and 333.45 nm, which is understood since the $^1Q_1$ absorption intensity in the v=1 and 2 spectra decays to zero for those photon energies (see Fig. 9). It is noted, however, that in the calculation of the distributions of Fig. 11 only one polarization direction of the linearly polarized laser electric field has been considered. When the opposite polarization direction is also considered, angular distributions which are the specular images with respect to θ_R=90° of the distributions of Fig. 11 are also obtained, and the final calculated distributions comparable to the experimental ones would be the average of these two specular images, which become symmetric with respect to θ_R=90°.

VI. DISCUSSION

The results presented in the previous sections show the high degree of qualitative agreement attained in this work between the experimental results and the theoretical calculations. The two mayor trends observed, namely, the increasing participation of initial vibrational states of CH_3I in both the $CH_3(\nu=0)$+I and $CH_3(\nu=0)$+I* channels and the increasing I/[I*+I] branching ratio with increasing photolysis wavelength, are well characterized by the dynamical calculations. However, there is a lack of quantitative agreement.

The correspondence between theory and experiment is even more apparent when the theoretical KEDs are convoluted with a broadening function to simulate the experimental apparatus response. In Fig. 12 the experimental KEDs are plotted jointly with the result of convoluting the theoretical curves with a Gaussian function (FWHM=741 cm^{-1}) in order to reproduce the width of the measured peaks. In this

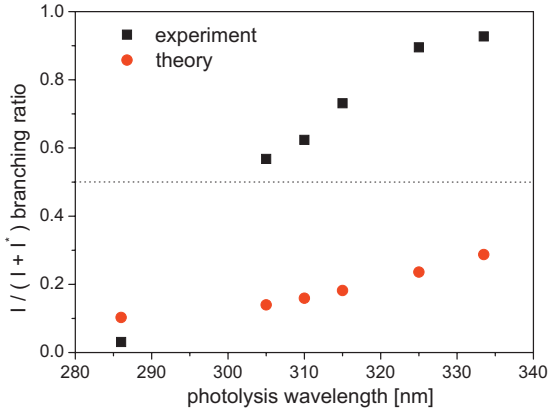

FIG. 13. Experimental and theoretical $I/[I^*+I]$ branching ratios obtained by integrating the kinetic energy distribution shown in Fig. 12. The horizontal dashed line at a branching ratio of 0.5 indicates the area where the I channel dominates over the I^* channel (top) and vice versa (bottom).

case, as in Figs. 7 and 8, a vibrational temperature of 255 K was used to weight the theoretical KEDs. Strikingly, the SO splitting in both sets of results takes the same constant value of ≈0.84 eV. This coincidence confirms that the experimental and theoretical KEDs peak at the same initial vibrational levels and that the product rotational distributions are similar in both cases. The difference in the experimental and theoretical values of the dissociation energy D_0 produces a small shift between both sets of KEDs, which is corrected simply by calibrating the experimental curves with the theoretical D_0 in Fig. 12. The experimental and theoretical curves show, as well, that the initial vibrational state contributions shift toward higher vibrational levels at higher photolysis wavelengths, being more acute this behavior for the CH_3+I^* channel. However, as can be predicted in Fig. 12 and clearly seen in Fig. 13, the main overall discrepancy between theory and experiment is in the $I/[I^*+I]$ branching ratios as photolysis wavelength increases.

Figure 13 plots the experimental and theoretical $I/[I^*+I]$ branching ratios as a function of photolysis wavelength. In both cases, all contributions from different initial vibrational states at each photolysis wavelength have been integrated to get the branching ratios. The dashed horizontal line in the figure at a branching ratio of 0.5 distinguishes the area where the I channel dominates over the I^* channel ($I/[I^*+I]>0.5$) from the area where the I^* channel dominates over the I channel ($I/[I^*+I]<0.5$). Only at 286.16 nm photolysis wavelength the experimental branching ratio is lower than 0.5. For the rest of photolysis wavelengths, the I channel dominates over the I^* channel. This is in strong contrast with what is obtained theoretically, where the I^* always dominates irrespective of the photolysis wavelength.

The grounds of the observed behavior lie in the absorption to and the dynamics on the three electronic states involved. In the center of the *A* band, at 260 nm, the absorption is mainly to the $^3Q_0$ state, which correlates with the I^* product. From the theoretical absorption spectrum shown in Fig. 10, at 286.16 nm the absorption to the $^3Q_0$ is 3 times stronger than the absorption to the $^3Q_1$ and 40 times than that to the $^1Q_1$. These differences and the observed anisotropies suggest that, at this photolysis wavelength, the dynamics is still ruled by the $^3Q_0$ state. The observed and calculated $I/[I^*+I]$ branching ratios for the $CH_3(\nu=0)+I$ channel at this wavelength are 0.03 and 0.1, respectively (see Fig. 13), which is already a factor of 3, the theoretical branching ratio being larger. The quantitative difference with what could be expected from the absorption spectrum is enhanced if we consider that the curve crossing between the $^3Q_0$ and the $^1Q_1$ surfaces populates the $CH_3(\nu=0)+I$ channel against the $CH_3(\nu=0)+I^*$ channel. Furthermore, the experimental values of $\beta\approx 2$ for the $CH_3(\nu=0)+I$ channel prove that the crossing is the only source of the I products at this wavelength. However, as can be seen in Fig. 10, a substantial contribution from $CH_3I(\nu_3=1)$ to the $CH_3(\nu=0)+I^*$ photodissociation channel is predicted theoretically at this photolysis wavelength in contrast with experiment.

Toward the red tail of the *A* band, the absorption to the $^3Q_1$ state increases, becoming greater than the absorption to the $^3Q_0$ state in the theoretical calculations at photon energies below 31 250 cm^{-1} (see the inset in Fig. 10). In this region the population in the $CH_3(\nu=0)+I$ channel grows with the photolysis wavelength and, consequently, both a $I/[I^*+I]$ branching ratio inversion (Fig. 13) and a change in the anisotropy of the $CH_3(\nu=0)+I$ channel (Table II) are observed experimentally and confirmed theoretically, although only in a qualitative way.

The present theoretical calculations, in agreement with what is observed experimentally, predict that the participation of vibrational excited states of the parent molecule grows for both the $^3Q_1$ and $^3Q_0/^1Q_1$ potential surfaces as λ_{phot} increases, but it does faster for the $^3Q_0/^1Q_1$ states. At 286.16 nm, not far from the center of the band, the hot CH_3I (only $\nu_3=1$) contributes through the $^3Q_0/^1Q_1$ states, mostly via the $^1Q_1\leftarrow{}^3Q_0$ curve crossing; at 305 nm, it is already visible a significant contribution from the $^3Q_1$ state (change in the anisotropy of the outer ring in Fig. 1) and at 333.45 nm, all the contribution for $\nu_3=0$ to the $CH_3(\nu=0)+I$ channel comes from the $^3Q_1$ surface, while the $^3Q_0/^1Q_1$ states is the only contribution from vibrationally excited CH_3I. This behavior reflects the increasing participation of the $^3Q_1$ state in the overall absorption spectrum toward its red tail.

We can think three possible reasons to explain the discrepancies found between theory and experiment. First, the wave packet calculations are carried out using a reduced dimensionality model for the CH_3I molecule in which the umbrella mode of the CH_3 fragment is modeled by a bond stretching (see Sec. III A). One can argue that this simplification can affect seriously the nonadiabatic dynamics between the $^3Q_0$ and $^1Q_1$ surfaces. Actually, recent femtosecond experiments where the reaction times into different channels yielding ground and vibrationally excited states of the umbrella mode of the CH_3 fragment were measured showed that the relative reaction times between the channels producing I^* and I decrease as vibrational excitation of the CH_3 increases, and this behavior could not be well reproduced by the wave packet calculations using the reduced dimensionality model.[2] However, the agreement found between experiment and theory is very reasonable when asymptotic properties, such as vibrational and rotational distributions of the CH_3 fragment or branching ratios, are con-

sidered. Therefore, in principle, one would not expect the reduced dimensionality approximation of the model to be the main reason of the large disagreement currently found between the experimental and theoretical branching ratios. Nevertheless, these previous comparisons have been carried out only at photolysis wavelengths close to the maximum of the *A* absorption band. The present work is actually the first which focuses in the red edge of the absorption band. We cannot rule out the possibility that the nonadiabatic crossing is not well reproduced by the wave packet calculations at photolysis wavelengths larger than 305 nm.

The second possible source of the discrepancies found between theory and experiment is the accuracy of the transition moments calculated for all three optically active surfaces as a function of R (the C–I distance).[47] Alekseyev and co-workers pointed out that transition moment calculations are much more sensitive to the quality of configuration interaction and SO treatments than are potential energies. High level *ab initio* methods were employed in Ref. 47 to obtain the mentioned transition moments as a function of R. Nevertheless, it is expected that the accuracy of the calculations diminishes as R increases. Large values of R correspond to larger photolysis wavelengths and, thus, a small percentage of error in the transition moments at large R may imply important changes in the absorption probabilities to the different potential surfaces involved in the red edge of the absorption band.

Finally, the third possibility is related to the relative absorption to the different potential energy surfaces in a region of a very low absorption cross section (see inset in Fig. 10). A change in the relative absorption to the $^3Q_0$ and $^3Q_1$ potential surfaces in this region may imply important consequences to the final branching ratios. The main factor driving this effect is the shape of the potential energy surfaces. In the *ab initio* calculations by Xie *et al.*,[45] where larger basis sets of triple-zeta quality and more SO configurations were used with respect to previous calculations by Amatatsu *et al.*,[43] the calculated total *A* band absorption spectrum still remains $\approx$1400 cm^{-1} higher and 800 cm^{-1} broader than the experimentally measured. In the most recent *ab initio* calculations by Alekseyev *et al.*[1,47] an adjustment consisting in a downward shift of the $^1Q_1$ potential energy surface by 900 cm^{-1} and of the total spectrum by 200 cm^{-1} had to be made for a better agreement with the experimental data. In the present calculations, we employed the $^1Q_1$ and $^3Q_0$ potential surfaces by Xie *et al.*[45] and the $^3Q_1$ potential surface by Alekseyev *et al.*[47] Small changes in the shapes and energetics of the potential surfaces involved can induce large changes in the relative absorption cross sections to the $^3Q_0$ and $^1Q_1$, especially in a region of very low absorption.

It is also possible that a combination of the three effects can explain the discrepancies, but we believe that it is the third reason which is the more plausible explanation. A better modeling of the CH_3I photodissociation should include wave packet calculations using a higher dimensionality model in which the CH_3 fragment umbrella mode is better modeled. However, the need of higher accuracy *ab initio* calculations of the potential energy surfaces is clear, at least in three dimensions, and the corresponding transition moments in order to reproduce the experimental results quantitatively.

VII. CONCLUSIONS

Slice imaging experiments have been carried out to study the photodissociation of CH_3I in the red edge of the *A*-band (286–333 nm) yielding CH_3 fragments in the ground vibrational state (ν=0) in correlation with $I(^2P_{3/2})$ and $I^*(^2P_{1/2})$. From the images, the $CH_3(\nu=0)$ kinetic energy and angular distributions have been extracted. The kinetic energy distributions show a vibrational structure, both in the $I(^2P_{3/2})$ and $I^*(^2P_{1/2})$ channels, corresponding to the contribution of CH_3I vibrational excitation in the ν_3(C–I) mode. The measured branching ratios, fragment anisotropies, and the contribution of vibrational excitation of the parent CH_3I have been rationalized in terms of the contribution of the three excited potential energy surfaces involved in the photodissociation process, i.e., the $^3Q_0$, $^1Q_1$, and $^3Q_1$, as well as the probability of nonadiabatic crossing between the $^3Q_0$ and $^1Q_1$ surfaces. Reduced dimensionality wave packet calculations, considering all the three excited potential energy surfaces, the corresponding couplings between them, and the available transition moments, have been carried out. Although the theoretical calculations reproduce the main experimental trends qualitatively, there is a lack of quantitative agreement, especially in the $I(^2P_{3/2})/I^*(^2P_{1/2})$ branching ratios. The discrepancies are explained in terms of small inaccuracies of the available potential energy surfaces in a region of a very low absorption cross section.

ACKNOWLEDGMENTS

We are very grateful to Professor T. N. Kitsopoulos for his help in setting up the pulsed slicing technique in our laboratory, to Professor A. B. Alekseyev for making available to us the *ab initio* potential energy surfaces and transition moments, and to Dr. Rebeca de Nalda for very helpful discussions. L.R.-L. thanks Consejo Superior de Investigaciones Científicas (CSIC) for a JAE-DOC contract under the Unidad Asociada "Química Física Molecular" between Departamento de Química Física I of UCM and CSIC. A.A. acknowledges financial support from the Spanish Ministry of Science and Innovation for a FPI fellowship. This work has been supported by FECYT (Ministerio de Ciencia e Innovación), Spain, Grant Nos. CTQ2008-02578/BQU and FIS-2007-62002 and Consolider Program SAUUL Grant No. CSD2007-00013. The Centro de Supercomputación de Galicia (CESGA) and the Red Española de Supercomputación (MareNostrum at BSC) are acknowledged for the use of their resources. The facilities provided by the Centro de Asistencia a la Investigación de Espectroscopia Multifotónica y de Femtosegundo (UCM) are gratefully acknowledged.

[1] A. B. Alekseyev, H.-P. Liebermann, and R. J. Buenker, J. Chem. Phys. **126**, 234102 (2007).
[2] R. de Nalda, J. Durá, A. García-Vela, J. G. Izquierdo, J. González-Vázquez, and L. Bañares, J. Chem. Phys. **128**, 244309 (2008).
[3] A. Gedanken and M. D. Rowe, Chem. Phys. Lett. **34**, 39 (1975).
[4] R. S. Mulliken and E. Teller, Phys. Rev. **61**, 283 (1942).
[5] G. Herzberg, *Molecular Spectra and Molecular Structure* (van Nostrand, Princeton, 1996).

[6] R. S. Mulliken, J. Chem. Phys. **8**, 382 (1940).
[7] R. S. Mulliken, Phys. Rev. **50**, 1017 (1936).
[8] S. J. Riley and K. R. Wilson, Faraday Discuss. Chem. Soc. **53**, 132 (1972).
[9] R. A. Hertz and J. A. Syage, J. Chem. Phys. **100**, 9265 (1994).
[10] R. Loo, H. P. Haerri, G. E. Hall, and P. L. Houston, J. Chem. Phys. **90**, 4222 (1989); R. Ogorzalek Loo, G. E. Hall, H. P. Haerri, and P. L. Houston, J. Phys. Chem. **92**, 5 (1988).
[11] M. Shapiro, J. Phys. Chem. **90**, 3644 (1986).
[12] M. D. Barry and P. A. Gorry, Mol. Phys. **52**, 461 (1984).
[13] G. N. A. van Veen, T. Baller, and A. E. de Vries, Chem. Phys. **97**, 179 (1985).
[14] W. K. Kang, K. W. Jung, D.-C. Kim, and K.-H. Jung, J. Chem. Phys. **104**, 5815 (1996).
[15] T. Donohue and J. R. Wiesenfeld, Chem. Phys. Lett. **33**, 176 (1975); J. Chem. Phys. **63**, 3130 (1975).
[16] P. Brewer, P. Das, G. Ondrey, and R. Bersohn, J. Chem. Phys. **79**, 720 (1983).
[17] S. Uma and P. K. Das, Chem. Phys. Lett. **241**, 335 (1995); J. Phys. Chem. **104**, 4470 (1996).
[18] S. L. Baughcum and S. R. Leone, J. Chem. Phys. **72**, 6531 (1980).
[19] W. H. Pence, S. L. Baughcum, and S. R. Leone, J. Chem. Phys. **75**, 3844 (1981).
[20] H. W. Hermann and S. R. Leone, J. Chem. Phys. **76**, 4766 (1982).
[21] T. F. Hunter and K. S. Kristjansson, Chem. Phys. Lett. **58**, 291 (1978).
[22] T. F. Hunter and C. M. Leong, Chem. Phys. Lett. **104**, 538 (1984).
[23] W. P. Hess, S. J. Kohler, H. K. Haugen, and S. R. Leone, J. Chem. Phys. **84**, 2143 (1986).
[24] D. H. Fairbrother, K. A. Briggman, E. Weitz, and P. C. Stair, J. Chem. Phys. **101**, 3787 (1994).
[25] A. V. Baklanov, M. Aldener, B. Lindgren, and U. Sassenberg, Chem. Phys. Lett. **325**, 399 (2000).
[26] A. T. J. B. Eppink and D. H. Parker, J. Chem. Phys. **109**, 4758 (1998).
[27] A. T. J. B. Eppink and D. H. Parker, J. Chem. Phys. **110**, 832 (1999).
[28] G. Li, H. J. Hwang, and H. C. Jung, Rev. Sci. Instrum. **76**, 023105 (2005).
[29] G. Li, Y. K. Shin, and H. J. Hwang, J. Phys. Chem. A **109**, 9226 (2005).
[30] G. Hancock, A. Hutchinson, R. Peverall, G. Richmond, G. A. D. Ritchie, and S. Taylor, Phys. Chem. Chem. Phys. **9**, 2234 (2007).
[31] A. Gilchrist, G. Hancock, R. Peverall, G. Richmond, G. A. D. Ritchie, and S. Taylor, J. Phys. Chem. A **112**, 4531 (2008).
[32] R. K. Sparks, K. Shobatake, L. R. Carlson, and Y. T. Lee, J. Chem. Phys. **75**, 3838 (1981).
[33] G. N. A. Van Veen, T. Baller, A. E. De Vries, and N. J. A. Van Veen, Chem. Phys. **87**, 405 (1984).
[34] T. Suzuki, H. Kanamori, and E. Hirota, J. Chem. Phys. **94**, 6607 (1991).
[35] H. Guo, Chem. Phys. Lett. **187**, 360 (1991).
[36] H. Guo, K. Lao, G. C. Schatz, and A. D. Hammerich, J. Chem. Phys. **94**, 6562 (1991).
[37] H. Guo, J. Chem. Phys. **96**, 6629 (1992).
[38] C. Rist and M. H. Alexander, J. Chem. Phys. **98**, 6196 (1993).
[39] A. D. Hammerich, U. Manthe, R. Kosloff, H. Meyer, and L. S. Cederbaum, J. Chem. Phys. **101**, 5623 (1994).
[40] M. Shapiro and R. Bersohn, J. Chem. Phys. **73**, 3810 (1980).
[41] H. Guo and G. C. Schatz, J. Chem. Phys. **93**, 393 (1990).
[42] Y. Amatatsu, K. Morokuma, and S. Yabushita, J. Chem. Phys. **94**, 4858 (1991).
[43] Y. Amatatsu, S. Yabushita, and K. Morokuma, J. Chem. Phys. **104**, 9783 (1996).
[44] M.-Y. Zhao, Q.-T. Meng, T.-X. Xie, K.-L. Han, and G.-Z. He, Int. J. Quantum Chem. **101**, 153 (2005).
[45] D. Xie, H. Guo, Y. Amatatsu, and R. Kosloff, J. Phys. Chem. A **104**, 1009 (2000).
[46] A. García-Vela and L. Bañares, Chem. Phys. Lett. **477**, 271 (2009).
[47] A. B. Alekseyev, H.-P. Liebermann, and R. J. Buenker, J. Chem. Phys. **126**, 234103 (2007).
[48] A. T. Eppink and D. H. Parker, Rev. Sci. Instrum. **68**, 3477 (1997).
[49] M. N. R. Ashfold, N. H. Nahler, A. J. Orr-Ewing, P. J. Vieuxmaire, R. L. Toomes, T. N. Kitsopoulos, I. A. Garcia, D. A. Chestakov, S. Wu, and D. H. Parker, Phys. Chem. Chem. Phys. **8**, 26 (2006).
[50] C. R. Gebhardt, T. P. Rakitzis, P. C. Samartzis, V. Ladopoulos, and T. N. Kitsopoulos, Rev. Sci. Instrum. **72**, 3848 (2001).
[51] V. Papadakis and T. N. Kitsopoulos, Rev. Sci. Instrum. **77**, 083101 (2006).
[52] A. B. Alekseyev (private communication).
[53] C. C. Marston and G. G. Balint-Kurti, J. Chem. Phys. **91**, 3571 (1989).
[54] G. G. Balint-Kurti and M. Shapiro, Chem. Phys. **61**, 137 (1981).
[55] G. G. Balint-Kurti, L. Füsti-Molnár, and A. Brown, Phys. Chem. Chem. Phys. **3**, 702 (2001).
[56] G. G. Balint-Kurti, R. N. Dixon, and C. C. Marston, J. Chem. Soc., Faraday Trans. **86**, 1741 (1990).
[57] G. G. Balint-Kurti, R. N. Dixon, and C. C. Marston, Int. Rev. Phys. Chem. **11**, 317 (1992).
[58] S. Hennig, V. Engel, and R. Schinke, J. Chem. Phys. **84**, 5444 (1986).
[59] F. Aguirre and S. T. Pratt, J. Chem. Phys. **118**, 6318 (2003).
[60] F. Aguirre and S. T. Pratt, J. Chem. Phys. **119**, 9476 (2003).
[61] V. Blanchet, P. C. Samartzis, and A. W. Wodtke, J. Chem. Phys. **130**, 34304 (2009).
[62] F. Wang, M. L. Lipciuc, X. Yang, and T. N. Kitsopoulos, Phys. Chem. Chem. Phys. **11**, 2234 (2009).
[63] R. N. Zare, *Angular Momentum: Understanding Spatial Aspects in Chemistry and Physics* (Wiley, New York, 1998).
[64] R. N. Dixon, J. Chem. Phys. **85**, 1866 (1986).
[65] T. P. Rakitzis and R. N. Zare, J. Chem. Phys. **110**, 3341 (1999).
[66] T. P. Rakitzis, Chem. Phys. Lett. **342**, 121 (2001).
[67] M. H. M. Janssen, D. H. Parker, G. O. Sitz, S. Stolte, and D. W. Chandler, J. Phys. Chem. **95**, 8007 (1991).
[68] R. Schinke, *Photodissociation Dynamics* (Cambridge University Press, Cambridge, 1993), p. 109.